Chapter 1 Production Target

1.1 Introduction

Production target design, Figure 1, has undergone significant evolution. Limited progress in producing a suitable radiation-cooled target has spurred interest in a water-cooling system with drastically lower operating temperatures. This system results in less than about five percent reduction in stopped muon yield compared to a similar radiation cooled unit. The theoretical and experimental research surrounding target design is discussed.

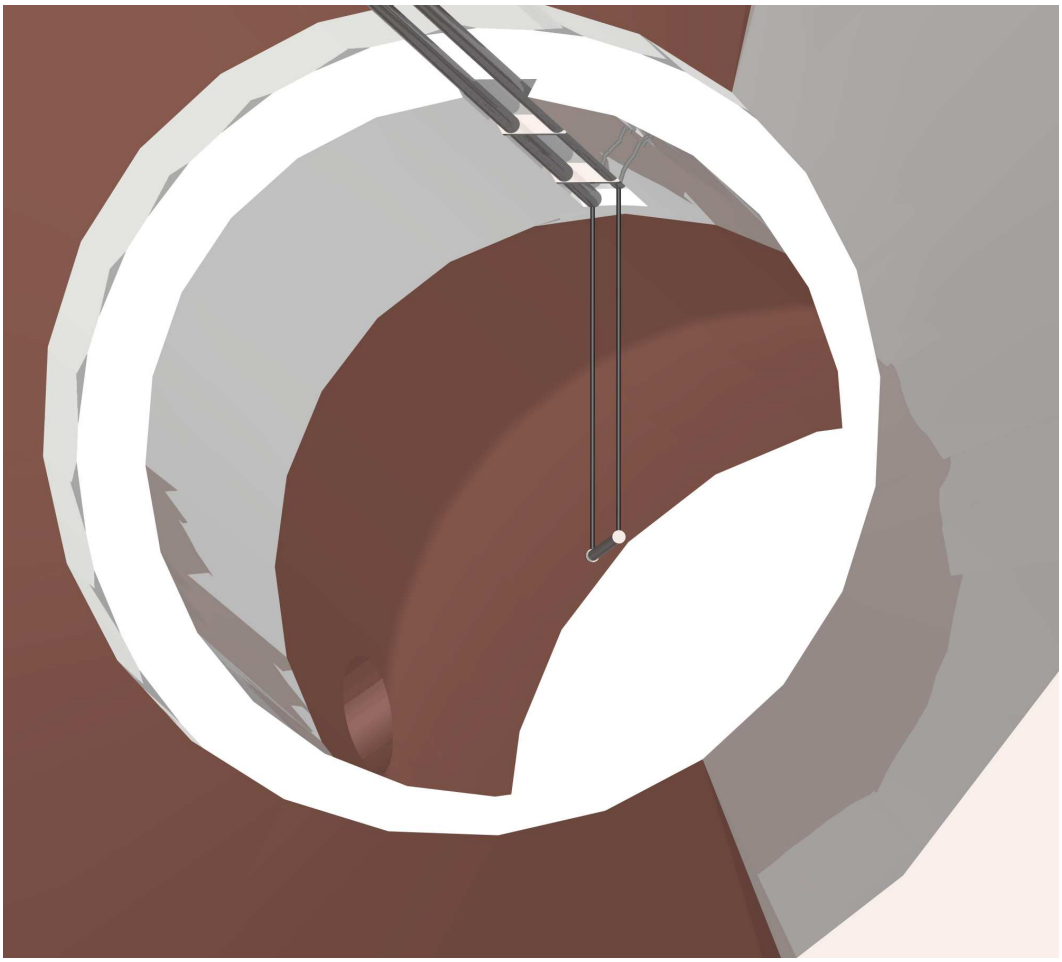

Figure 1: MECO production target installed in the Production Solenoid. The water-cooled design is shown here, viewed at the upstream end of the muon beamline. The entrance of the proton beam is the opening in the heat and radiation shield seen left of center and nearer the bottom of the figure.

Negative muon production is accomplished by directing a high-intensity 7.5 GeV proton beam onto a small dense metal target, nominally the size and shape of a pencil, located within a solenoid with an axially graded magnetic field. Approximate target position is indicated by the black star in Figure 2. The primary beam strikes the target end-on to produce pions that decay into muons. The proton beam is pointed in the direction of increasing field intensity so that charged secondaries spiral along in a magnetic bottle towards the "closed end", reflecting many charged particles back towards the Transport solenoid entrance, thus collecting pions over a large solid angle. A similar system was discussed by Djilkibaev, Lobashev, & collaborators [1, 2], and their ideas were later adopted by proponents of the muon collider [3].

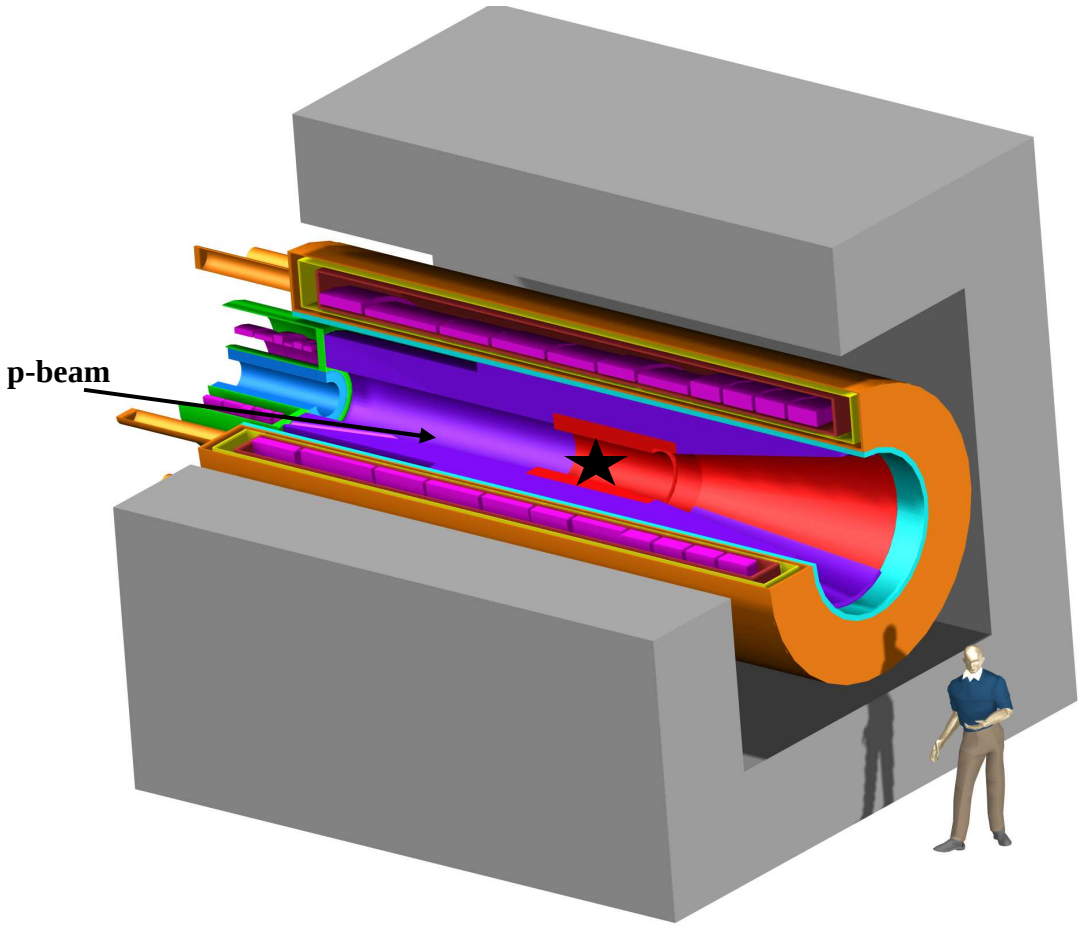

Figure 2: MECO Production Solenoid; the grey structure is the iron return yoke. The interface to the Transport Solenoid can be seen at the left.

In particular, pions produced in the target with transverse momentum below ~180 MeV/c travel in helical trajectories within the clear bore of the solenoid and decay to muons. Invariance of the quantity p_t^2/B and energy conservation imply that charged particles moving towards the closed end of the "bottle" are reflected down stream if

$$\sin(\theta) > \sqrt{B_{target} / B_{max}},$$

where B_{max} and B_{target} are the values of the axial component of the magnetic field at the target and the upstream end, respectively, and θ is the angle of the pion with respect to the solenoid axis at the target. For the production region magnetic field values, the loss cone, where particles are not reflected, has a half angle of about 30° giving a solid angle acceptance for pion capture ~93%. The transport solenoid filters the beam for unwanted particles and passes what remains to the stopping target.

To set the scale, a radiation-cooled target is a tungsten cylinder 16 cm long and 4.0 mm in radius weighs about 155 g and receives an instantaneous on-peak power of 10 kW, i.e., a time average of 5 kW. Production of some 10^{17} stopped muons in the planned 30-week running time requires that MECO aim 4×10^{13} protons/sec at the production target. The AGS is especially suited to provide the required beam energy and intensity, along with a pulsed microsecond time structure and high beam extinction between pulses, features crucial to rejecting two kinds of background. The target-heating scenario is dictated by the macroscopic time structure of the beam; namely, the AGS cycle time of one second and duty factor 0.5.

The average number of muons reaching the stopping target per incident proton depends on many factors. Critical to achieving a high stopped muon yield, we must collide protons on a target with as large an atomic number and density as possible. Yield, as well as cooling, depends on target geometry, position and orientation. More generally, muon yield is sensitive to solenoid design and material anywhere in the clear bore of the magnet. Hence, the target, cooling system, and mechanical support must be compact and introduce little additional mass beyond that of the target, thus minimizing pion reabsorption. The target mounting must be sufficiently insensitive to vibrations to maintain good positioning. Furthermore, temperature must be controlled to avoid operating too close to the melting point and avoid thermal stress levels that may lead to mechanical failure or geometrical distortion. Still other factors contribute to the stopped muon yield, which are discussed elsewhere in this document; e.g., proton beam energy, production and transport solenoid fields, and the design of the collimators used to select muons of the appropriate momentum and charge.

1.2 Muon Production

The basic principle of the production region is illustrated in a GEANT simulation, Figure 3, showing a view of the production and beginning of the transport solenoids. Design of the production solenoid calls for a graded magnetic field with maximum intensity of the axial component to be 5 T at the upstream end, decreasing linearly to 2.5 T. The target is a16 cm long, pencil-sized cylinder and has its axis tilted away from that of the solenoid to intercept the proton beam. The direction of this beam is opposite that of the muon beam in order to reduce the fluence of low energy photons and neutrons into the muon channel and eliminate complications associated with the interactions of the diffuse exiting proton beam and the beginning of the muon transport. A collimator of radius 15 cm, visible in the figure, defines the entrance to the transport solenoid.

Tungsten is a suitable target material for initial studies comparing various cooling schemes; it has a high density, 19.3 g/cm^3, good refractory properties, and a large pion production cross-section. Tungsten has the highest melting point, ~3683 K, and thermal conductivity of all pure-metal refractories. In addition, this metal has good mechanical stability at high temperature, with yield strength about 5800 psi at 2000 K, and modest thermal expansion coefficient 6.01×10^{-6} K at 3000 K.

The calculated values of particle fluxes in the beam are based on GEANT simulations of proton interactions in a tungsten target. GEANT has a variety of hadron interaction codes, and we have primarily used GHEISHA. However, there is significant variation between different codes for the total π^- production cross-sections and kinematic distributions. For example, the GHEISHA and FLUKA codes differ by a factor ~4 in the muon yield at 8 GeV incident proton energy; the variations with model were discussed extensively in the original MECO proposal [4]. In order to reduce the uncertainty in the muon yield (and hence the sensitivity of the experiment) due to the uncertainty in the hadronic models of low energy hadron production, we have scaled the results from GEANT (with GHEISHA) by a factor determined from comparison with measured π^- production cross sections in proton tantalum interactions. The effect of this scaling is to reduce yields by a factor of ~2 with respect to the GEANT + GHEISHA prediction. The backgrounds that depend directly on pion production rates have also been scaled in the same way.

The data to which we compare our simulation are from interactions of 10 GeV/c protons with tantulum, which is adjacent to tungsten in the periodic table. Measurements [5] include the invariant cross sections for π^- production as a function of pion kinetic energy T and production angle θ measured in the reaction $p^+\mathrm{Ta} \rightarrow \pi^- + X$ over the full angular production range and for $p_\pi > 80$ MeV/c. One mm thick Ta plates with spacing of 93 mm were placed in a 2 m propane bubble chamber that was operated under a magnetic field of 1.5 T. Pion trajectories were confidently identified with minimum momentum of 80 MeV/c (T = 21 MeV). The measured average π^- multiplicity at 10 GeV/c is 1.51 ± 0.03. The experimental π^- inclusive differential cross section measurements, together with a phenomenological fit, are shown in Figure 4. The dependence of the invariant cross sections on the π^- kinetic energy is well approximated by an exponential function: $f = C \exp(-T/T_0)$. The total pion production cross section for Ta at 10 GeV/c found by integrating this formula with fitted values of C and T_0 is 2.36 barn. With a nuclear inelastic cross section for Ta of 1.56 barn, there is good agreement with the measured pion multiplicity of 1.51.

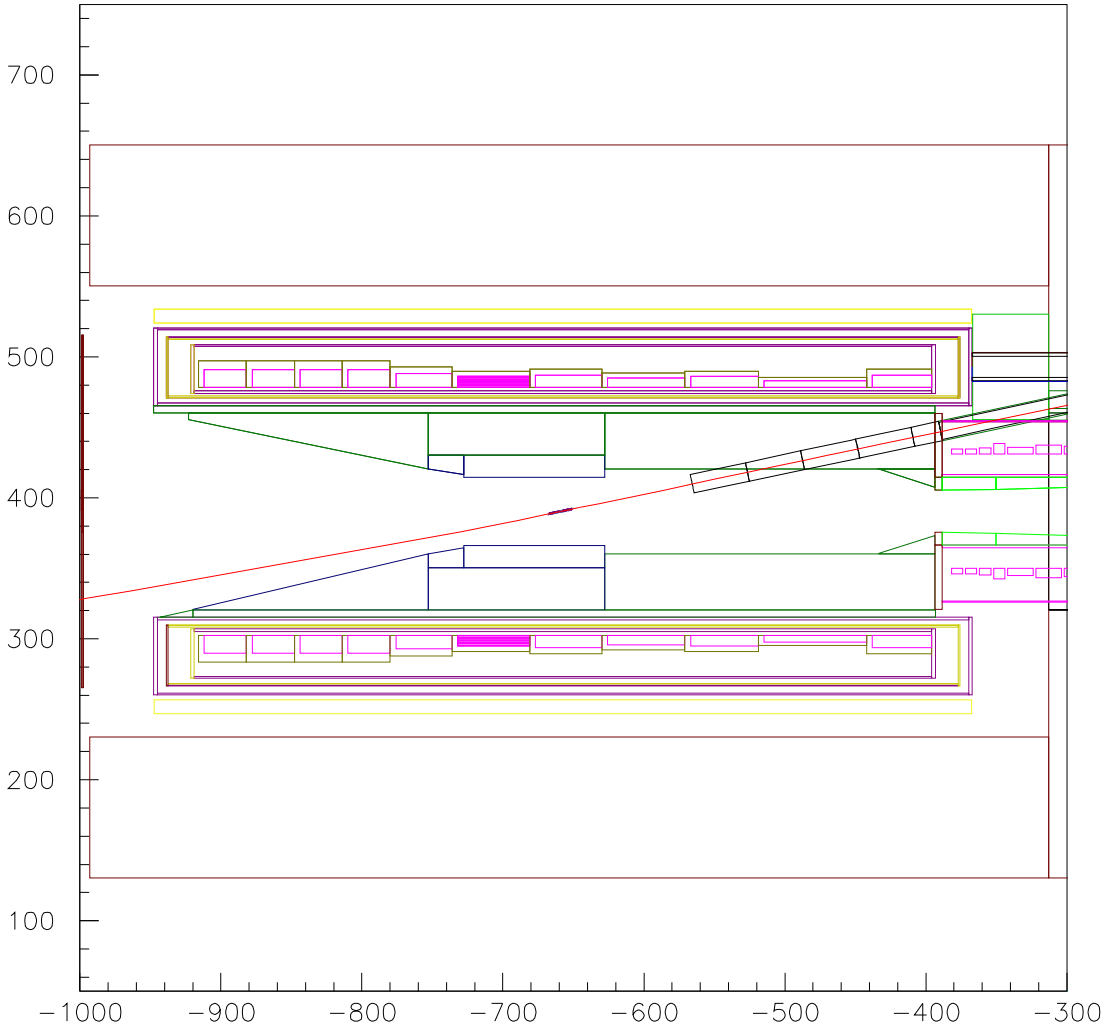

Figure 3: GEANT simulation of Production Solenoid; cross-section, viewed from above. Note that coordinates are in centimeters. The AGS beam enters from the right, strikes the target at approximately (-650 cm, 400 cm), and exits through a thin window at the lower left.

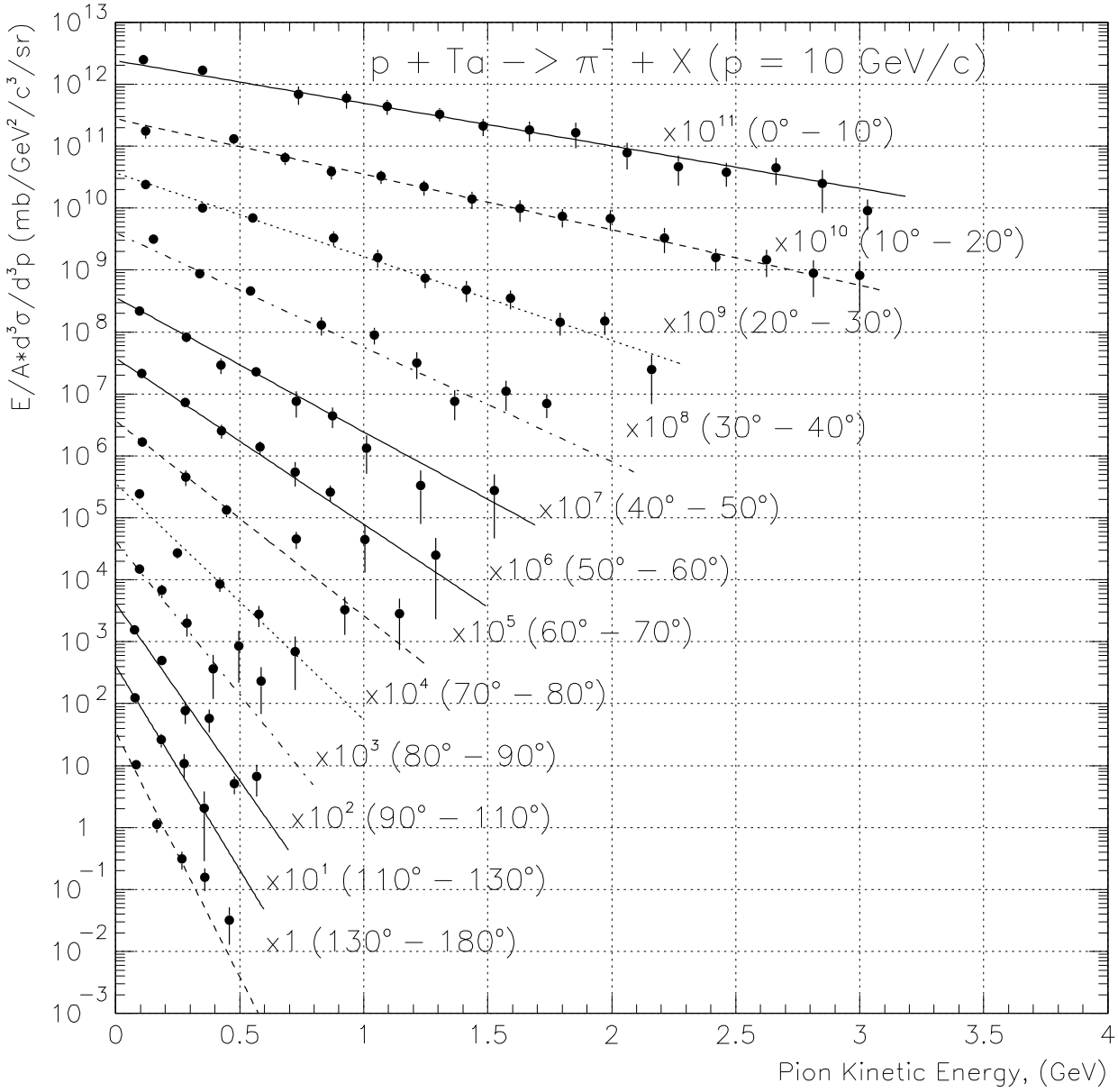

Figure 4: Negative pion inclusive differential cross section in different angle intervals for 10 GeV/c protons incident on tantalum [5]. The lines are the result of a fit to an exponential form: $f = C\exp(-T/T_0)$.

To compare the MECO muon flux simulation using the hadron codes with the experimental data, a Ta proton target (ρ = 16.6 g/ cm^3) with length 19.34 cm (1.67 nuclear lengths) and radius 0.4 cm was studied. For the muon flux calculations, the GEANT 3.21 code with the GHEISHA hadronic model was used. A proton beam with Gaussian shape and $\sigma_x = \sigma_y$ = 0:2 cm was caused to impinge on the target. The proton interaction point was chosen using GEANT, and then π^- were produced at that point according to the measured production cross sections. The π^- where then tracked using the GEANT code and the resulting μ^- yield calculated. The ratio of this μ^- yield based on measured production cross sections to that based on GHEISHA is 0.54. We scale all results that depend on pion yield at 8 GeV/c down by a factor of 2 to account for this difference and the energy dependence of the production cross section, the latter taken from a GEANT calculation.

As previously mentioned, and here in more detail, the yield of muons depends on the target shape, the proton energy, the value of the field in the production and transport solenoids, the clear bore of the production solenoid, and the size of the collimators. The yield was optimized [6, 7] with respect to variations in these parameters. It is relatively insensitive to small variations in target position and to the target length in the range of 12-20 cm. The yield decreases by about a factor of two with target radius variations between 3 mm to 9 mm due to absorption as the pion exits the target and as it passes through it again while moving in a helical trajectory in the production solenoid. We currently use a target radius of 3 mm. This has some implications on target heating, as discussed below. In addition to being necessary because of the incoming proton beam angle, the target tilt also helps reduce scatter of pions following a helical trajectory. For a 5 T maximum field in the production solenoid and a 15 cm radius collimator, the muon yield decreases by only ~3% in going from a 30 cm to 20 cm radius clear bore. This region may thus be available should more shielding be necessary. To reduce pion loss, the target support structure should also be as low in mass as possible.

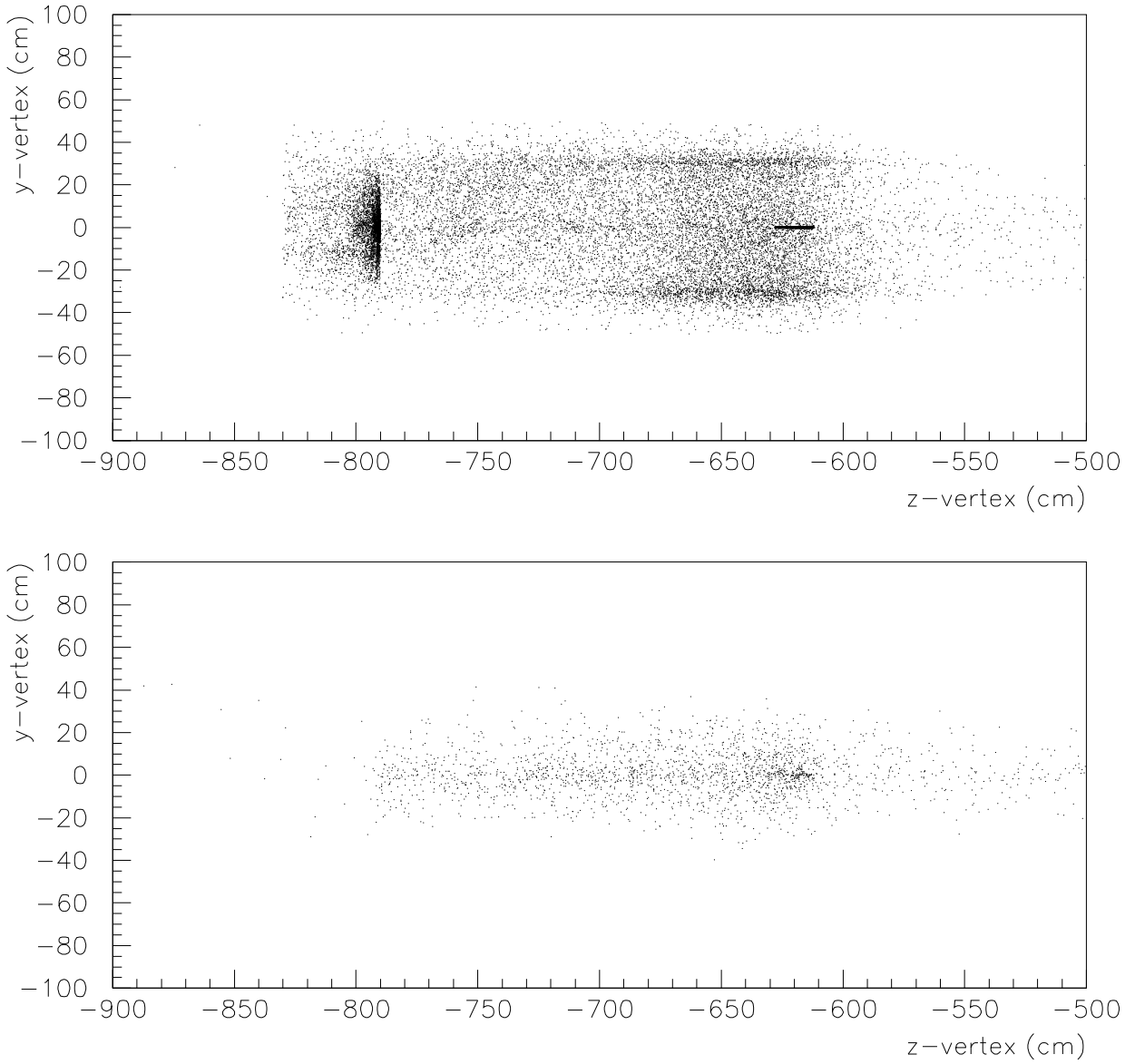

Figure 5: Distribution of positive (top) and negative (bottom) muon creation points in the Production Solenoid. Most positive muons are generated in the walls of the solenoid, surface muons, whereas negatives are largely from negative pion decay in flight.

1.3 Target Heating

The use of a heavy target in a very intense proton beam requires careful consideration of target heating. The power deposited in the target is determined from a GEANT simulation; it is not very sensitive to the hadronic code used. Table 1 shows the GEANT [8] simulation results for average energy loss per proton and heat release in the target for 8 GeV/c protons. The calculated average energy loss per proton is equal to ~0.7 GeV/proton and ~0.8 GeV/proton for target lengths 16 cm and 20 cm, respectively, equivalent to a peak power of 9.4 kW and 10.2 kW. The longitudinal distribution of the average energy loss per primary 8 GeV/c proton is shown in.

Table 1: Average energy loss per proton and power delivered to a tungsten target by an 8 GeV/c proton beam with emittance 6pi-mm-mrad. An average of 40 Tp per one second machine cycle was used.

Hadron Code	Target Radius (cm)	Target Length (cm)	Average Loss (GeV)	Peak Power (kW)	Average Power (kW)
GHEISHA	0.4	16	0.7	9.4	4.7
GHEISHA	0.4	20	0.8	10.2	5.1
FLUKA	0.4	16	0.7	9.4	4.7
FLUKA	0.4	20	0.8	10.2	5.1
GHEISHA	0.6	16	1.0	12.8	6.4
GHEISHA	0.6	20	1.1	14.0	7.0
FLUKA	0.6	16	1.0	9.4	6.4
FLUKA	0.6	20	1.1	10.2	7.0

The data in Table 1 was used in design calculations for radiation cooling. Based on later studies comparing the effect of a water-cooling system on stopped muon yield to that of radiation-cooled, see Figure 7 and [9], target radius was re-optimized to 3.0 mm. Subsequent to this, energy deposition was re-evaluated, leading to a total instantaneous power of 7550 Watts; Figure 6 shows the results of these calculations in more detail.

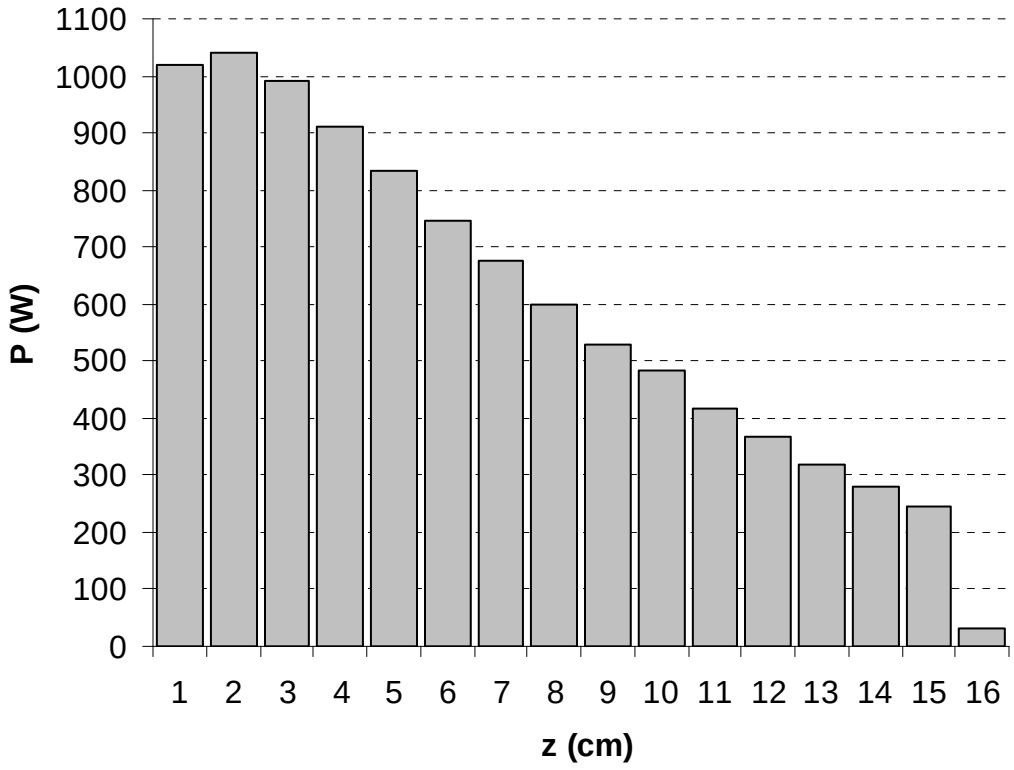

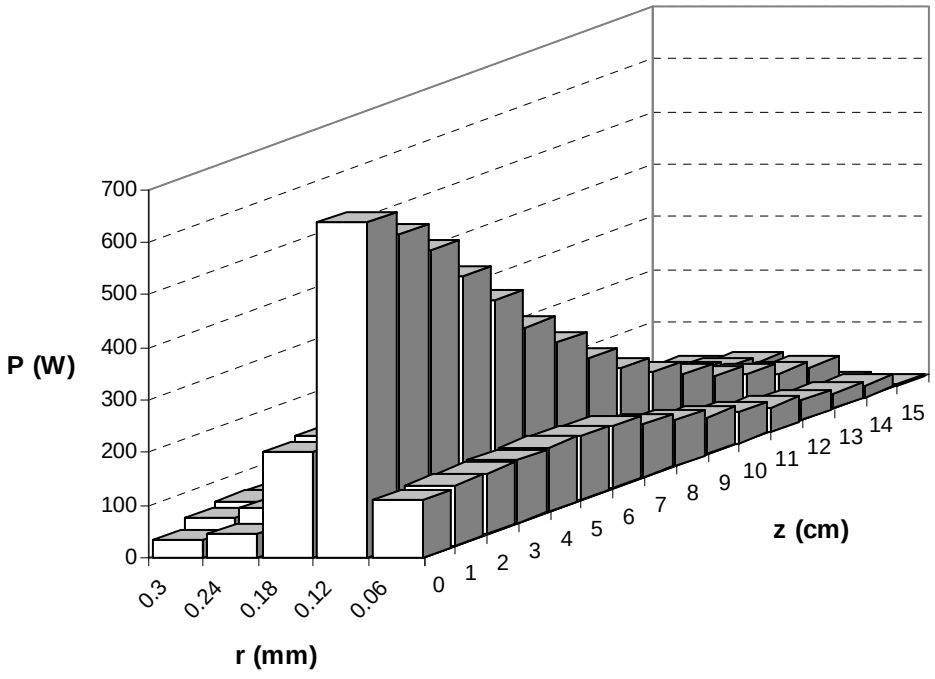

Figure 6: Power distributions for MECO target with 3.0 mm radius and 16 cm length cylinder. Nota bene: These are the distributions used in cooling calculations, scaled to 9500 Watts total instantaneous power, the actual GEANT value is 7550 Watts.

1.4 Stopped Muon Yield

Target geometry re-optimization. A study of how stopped muon yield depends on radius reveals that the optimum target radius is now, 3.0 mm, see Figure 7. Turning to the relationship between target length and yield, Figure 8 shows that 16 cm is still a reasonable target length. We will learn more about possible target geometry modifications after studying the relationship between target pressure drop and flow rate.

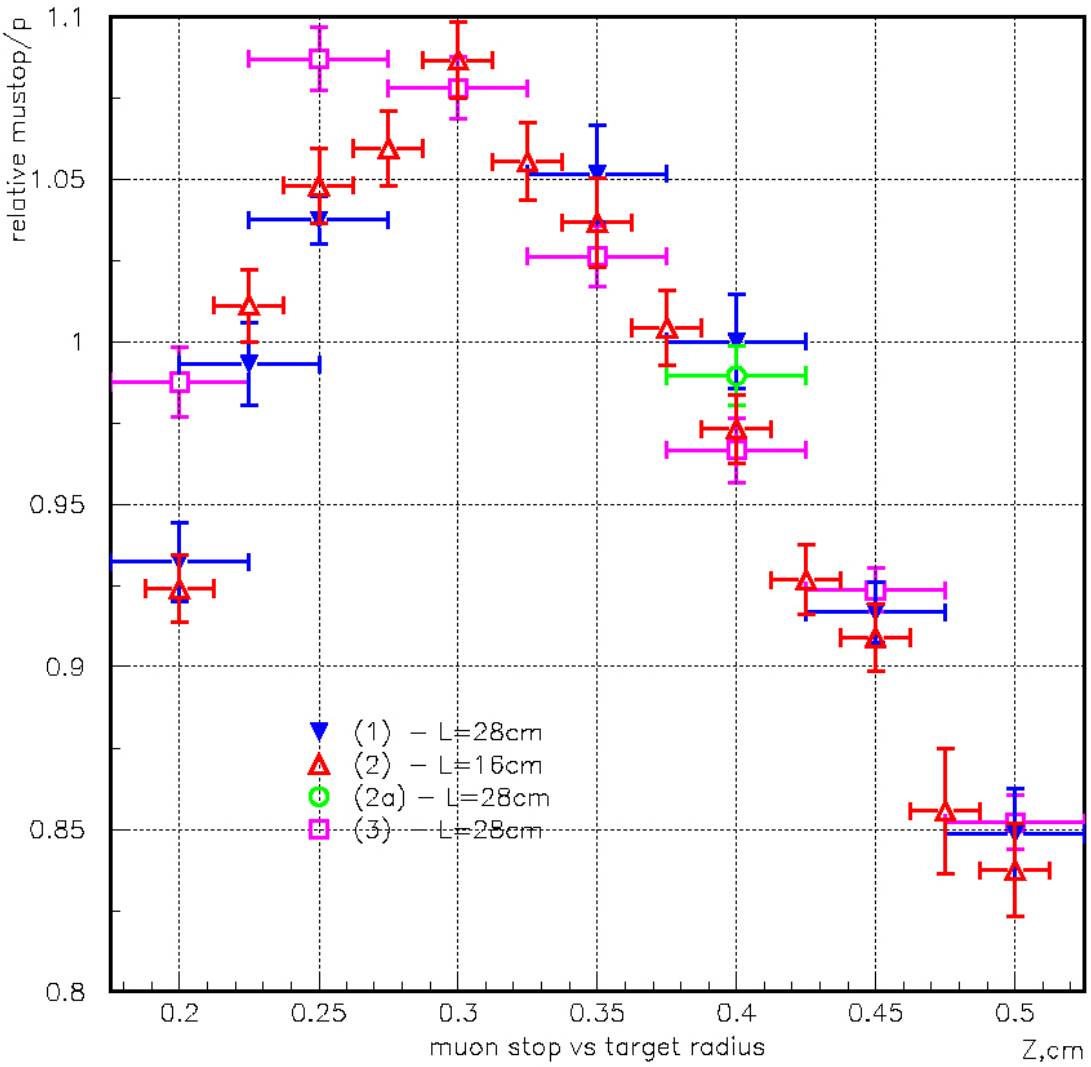

Figure 7: Stopped muon yield per primary proton versus target radius for a water-cooled target. Yield is reported relative to that for radiation cooling; Figure 5 of [9].

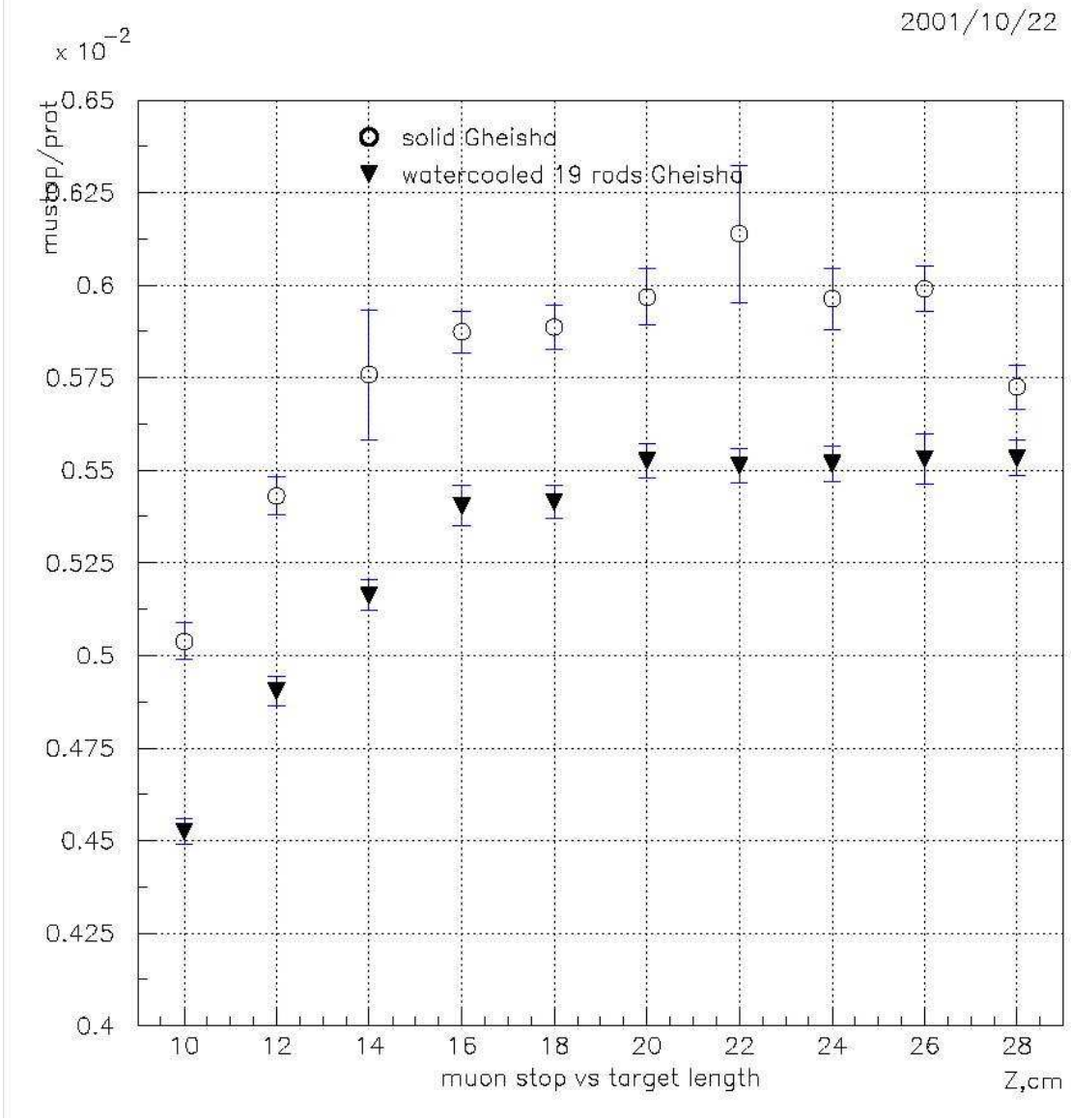

Figure 8: Relative stopped muon yield per primary proton vs target length; Figure 8 of [9].

The first entry in Table 2 is for similar to a radiation-cooled target, except for the presence of the inlet and outlet tubes. Current design of the water-cooled system calls for a gap size of 0.3 mm.

Table 2: Optimization of stopped muon yield as a function of coolant containment shell thickness and gap size.

Water Thickness (mm)	Ti Wall Thickness (mm)	μ^-- Stops per Proton	Acceptance Loss (%) (+/- 1.5)
0	0	0.0050	0.0
0.5	0.5	0.0048	4.6
0.25	0.15	0.0048	4.1
0.2	0.15	0.0049	2.7
0.3	0.15	0.0048	4.5
0.4	0.15	0.0047	5.8
0.5	0.15	0.0047	6.3
0.25	0.2	0.0048	4.5
0.25	0.3	0.0047	6.7
0.25	0.4	0.0047	6.0
0.25	0.5	0.0047	5.4
2.35	0.76	0.0037	27.0
0.5	0.3	0.0041	17.8

1.5 Target Cooling

Two cooling strategies have received significant study: *radiation* and *forced convection* with water as the coolant. Radiation cooling is attractive because it provides a high muon yield, is simple to operate and virtually maintenance-free. On the other hand, high operating temperatures lead to evaporation of some of the target material; requiring strategies to control contamination of the rest of the muon beam line and detector area, and require good control of thermal stresses. Convective cooling makes drastically lower operating temperatures possible, extending the possibility of achieving even greater muon beam intensities. An essential requirement for such a system is to maintain a non-boiling condition, since gas formation would impede flow through small water channels. This type of cooling provides more latitude in selecting target materials with higher densities and thermal conductivities, thus raising the possibility of reduced thermal stresses and an increased useful lifetime of the target. However, this cooling system requires greater maintenance, and significantly more system design consideration. Protocols for coolant storage and disposal would be required.

1.5.1 Radiation

The design currently under consideration consists of…thin tungsten wires to hold the target in place, with a system of springs designed to take up the mm scale slack produced when the wires expand upon heating. Using radiation alone to cool the target also minimizes absorptive material. This puts stringent constraints on possible target geometry.

The temperature and stress distributions were computed using ANSYS, including a realistic power distribution. This calculation shows that a single cylinder is not mechanically stable under these conditions because of stresses induced by longitudinal and radial temperature gradients.

Significant reduction of target temperature can be achieved in several ways: segmenting the target to increase the radiative area and decrease radial temperature gradients, use of a high emissivity coating, and using a more uniform beam profile to decrease radial temperature gradients.

Table 3: Thermal and mechanical properties of tungsten as function of temperature. Displayed here are: thermal conductivity κ, specific heat at constant pressure c_p, coefficient of linear expansion α, modulus of elasticity E, and the elastic limit, designated here as the yield point σ_{Yield}. The total emissivity of tungsten is temperature dependent; however, for this study it is held fixed at 0.43. The melting point of tungsten is the highest of all pure refractory metals, 3683 K.

T (K)	300	500	1000	1500	2000	2500	3000
κ (W/cm K)	1.6	1.4	1.25	1.1	1.006	0.9	0.85
c_p (J/g K)	0.1313	0.1380	0.1465	0.1570	0.1723	0.1946	0.2255
α (10^{-6})	0	4.04	4.42	4.82	5.22	5.61	6.01
E (MPa)	41.0	38.0	36.0	34.0	32.0	28.0	23.0
σ_{Yield} (MPa)	1519	150	110	75	40	20	NA

A simple lumped thermal analysis of radiation cooling illustrates the gross behavior of local target temperature. Non-uniform heating and a finite thermal conduction time do not radically distort the temporal features we wish to point to: namely, the warm-up time and small oscillations about a constant time-average temperature after times large compared to the warm-up time. In Figure 9, the target begins at room temperature, and then the heating starts. The black oscillating line is the instantaneous temperature, and the red line is the cycle-averaged temperature. For comparison, we include the solution for a continuous (not pulsed) power source of the same intensity.

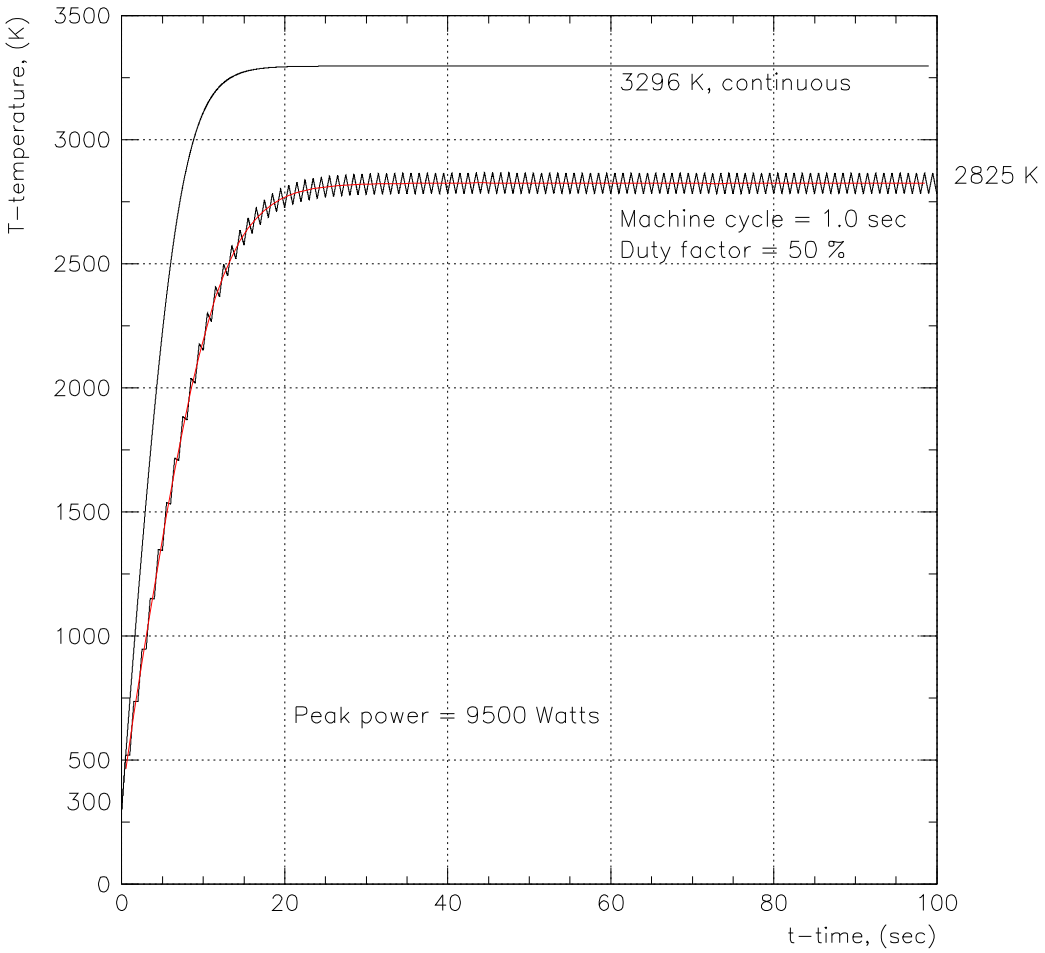

Figure 9: Numerical solution to lumped heating equation, including the temperature dependence of the specific heat and emissivity. For an 8 GeV/c proton beam delivering 40 Tp in each one-second cycle, with duty factor 0.5, the instantaneous power for a 16 cm long, 0.4 cm radius tungsten rod is 9500 Watts.

ANSYS calculations were performed using realistic conditions, including the spatially non-uniform, pulsed power distribution expected for MECO assuming the same target geometry and conditions explained in the caption of Figure 9. Both on- and off-spill temperature distributions are given in Figure 10. Figure 11 shows the distribution of Von Mises stresses.

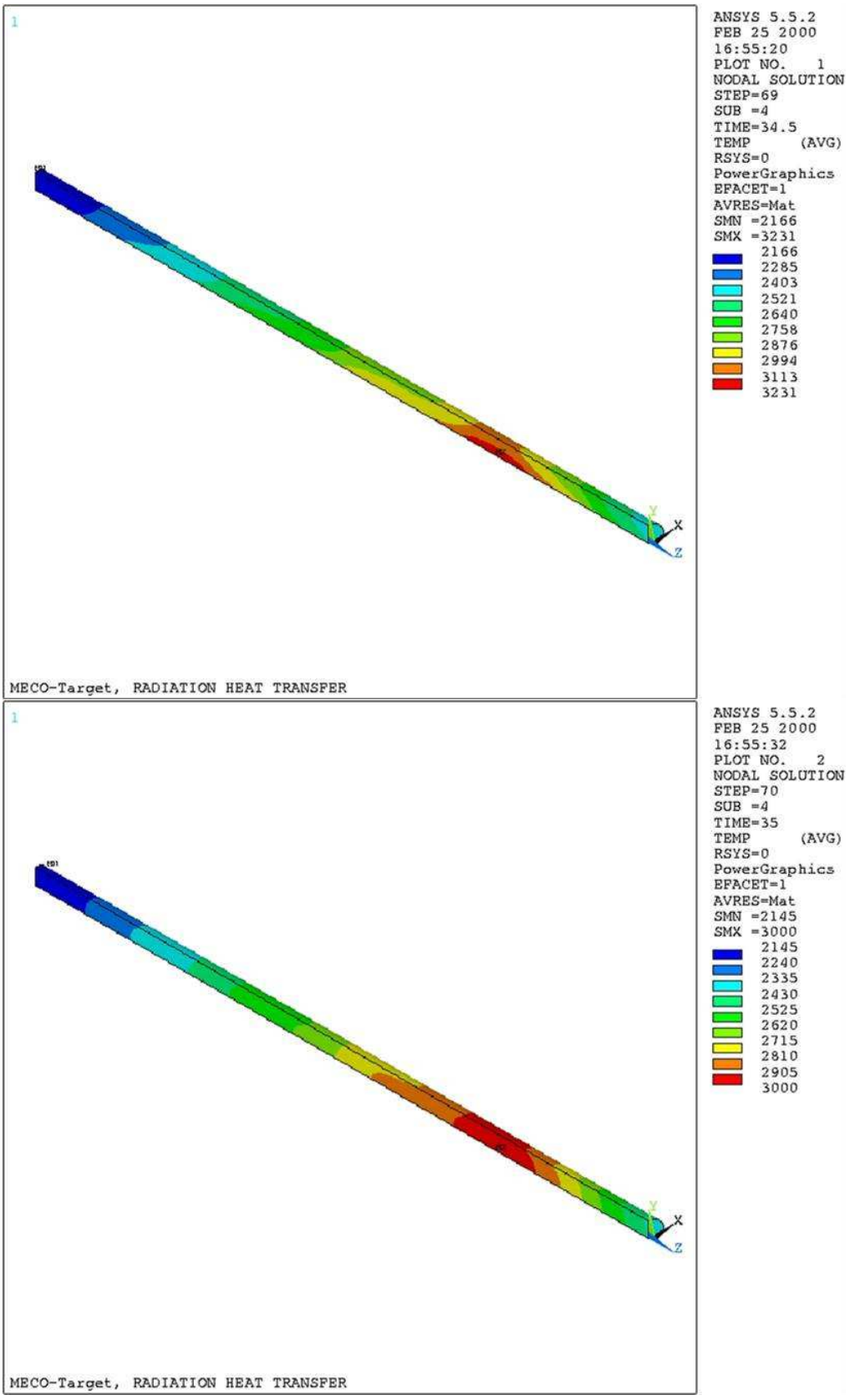

Figure 10: Temperature on-spill (top) and off-spill (bottom), in Kelvins.

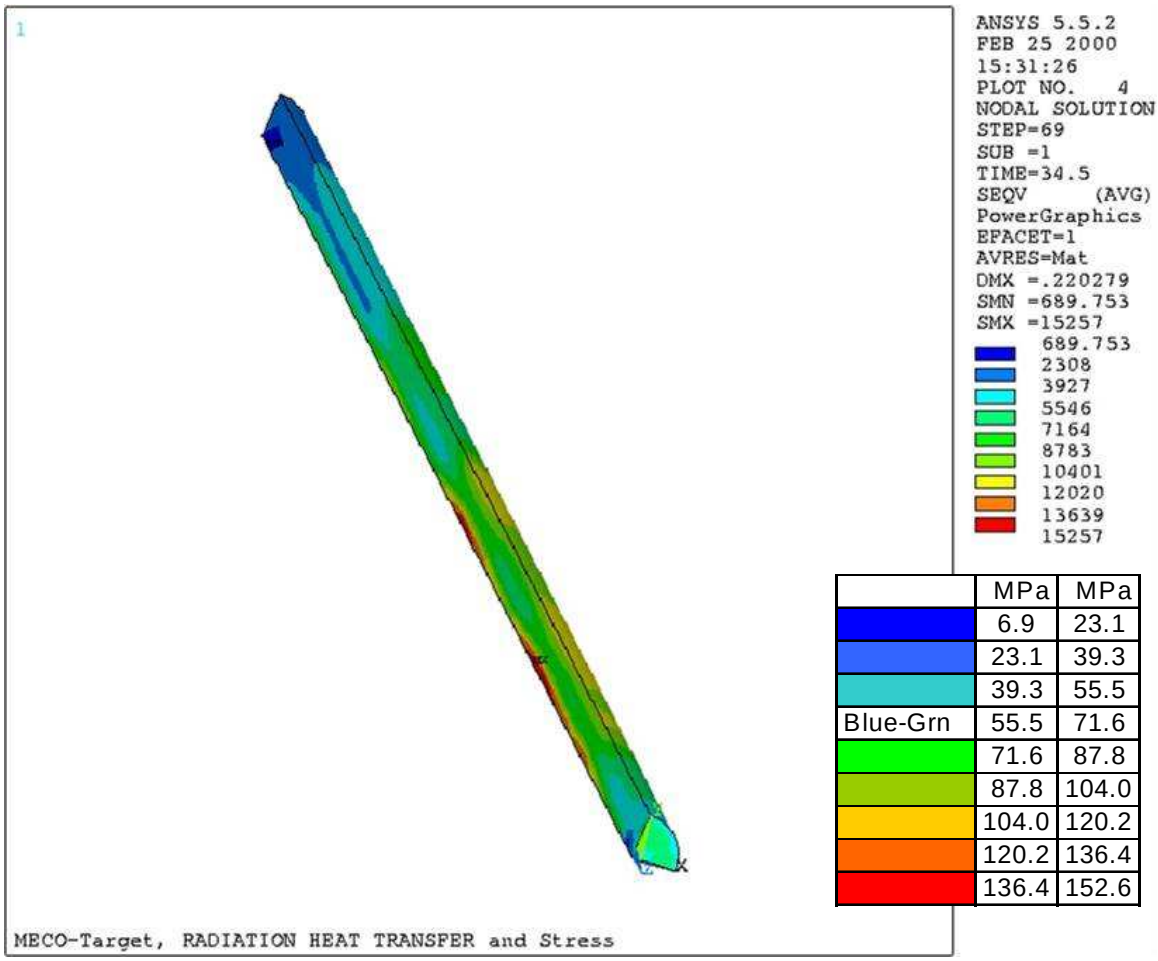

Figure 11: On-spill, Von Mises stress in N/cm^2. Tungsten rod, radius 4 mm and length 16 cm.

Tungsten surfaces with higher emissivity (~0.9) have been formed using methods such as chemical vapor deposition. We are exploring with engineers at BNL and materials scientists at the College of William and Mary whether this type of surface can be prepared on a solid tungsten cylinder. The use of materials other than tungsten for the surface cating is also being considered. Such coatings also have the advantage of eliminating oxidation of the tungsten surface in the unlikely event of catastrophic loss of vacuum while the target is hot.

To minimize absorption of π^- in support material in the production solenoid the target would be suspended suspended in position with very low mass supports. Tungsten's high melting point makes a radiation-cooled target possible even with the very high proton flux and resulting energy deposition.

The power distribution along the length of the MECO target is peaked within the first two to four centimeters and slowly decays over the remainder, a feature reflected in the temperature distribution shown in Figure 10 for an early target design. The radial power distribution in this figure was approximated with a Gaussian. Note that the maximum core temperature near the power deposition peak is 3231 K, with a surface temperature there of 3113 K.

Thermal stress analysis of the radiation-cooled single solid cylinder has shown that this geometry is mechanically unstable. Redesign efforts aimed at reducing operating temperature and thermal stresses have sought to add high emissivity coatings, divide the target into thin slices & space them out along the beam, and adding to these smaller pieces slots both along & perpendicular to the target axis. The results of this investigation have produced a significantly reduced operating temperature, with the maximum between 1977-2032 K on spill. This target consists of 2.0 mm slices, spaced by 8.0 mm along the beam, assuming the surface is treated to obtain an emissivity of 0.9. Unfortunately, this modification of a single rod makes the length of the target unacceptable, due to the increased complexity of the supports and greater probability for pion reabsorption. Research on radiation cooling continues.

The structural analysis used many different prototype target types each of which consisted of 16 cm long tungsten divided into pieces whose thickness and separation were varied. All of the targets have a radius of 0.4 cm. The emissivity of the target and the beam profile (uniform or a gaussian of σ = 0.2 cm) were also varied. The properties of tungsten, the description of a subset of target models and the results of the calculation are presented in Table 4. **Error! Reference source not found.** shows the results for a target consisting of 0.4 cm disks separated by 0.8 cm.

As can be seen in the table, it is possible to obtain, with a small enough disk thickness and large enough spacing, a target which is mechanically stable under our beam conditions.

The Von Mises stress criterion is also know as the maximum distortion energy critierion; in this picture, failure occurs when the potential energy of distortion reaches the same value as in yield under uniaxial tension. The Von Mises stress is less conservative than other commonly used measures, such as the maximum sheer stress criterion.

Table 4: Target stresses and temperatures, on-spill, for a radiation-cooled tungsten target separated into slices and spread evenly along the length by 0.8 cm. Temperature and stress dependence on slice thickness and emissivity are shown here. The radiation form factor for each slice was 0.87 and the radial energy distribution is modeled by a Gaussian. The "warm-up time" given here is the characteristic time to reach a constant cycle-averaged temperature distribution. The stress values given are the maximum compression and tension values found for each target. In a cylindrical coordinate system, with the target axis along z, "axial" stresses are oriented along z, "hoop" stresses are in the theta direction, and radial stresses are along a radius. The Von Mises stress is explained in the text.

Trail number	6	7	8	9	10	11	12
Thickness (cm)	0.8	0.4	0.4	0.2	0.1	0.4	0.4
Emissivity	0.9	0.4	0.9	0.9	0.9	0.9	0.9
Warm-up time (sec)	14	16	14	12	10	14	14
Max. temperature on-spill (K)	2396	2705	2236	2032	1803	2271	2285
Stresses (Mpa)							
Axial	85.9	18.1	18.2	2.5	1.1	13.5	115.4
	-95.3	-20.5	-20.0	-2.5	-0.7	-23.7	-37.8
Hoop	94.6	73.7	71.5	44.2	31.2	105.1	105.7
	-83.7	-74.6	-72.4	-45.0	-30.0	-44.9	-26.9
Radial	44.7	23.7	23.8	1.9	1.0	58.3	34.2
	-87.3	-74.5	-72.2	-45.0	30.1	-44.9	-27.0
Von Mises	82.8	70.1	67.7	43.5	30.7	89.1	95.3

However, these targets are longer overall than is desirable. We are currently investigating a tapered target consisting of smaller radius disks upstream. This will result in smaller radial stresses due to target size where the energy deposit is largest, but allow larger radii downstream where the beam has spread due to multiple scattering.

Overall, moving the beam position over the target to obtain greater uniformity in heating [10] can reduce stresses; this subject has been studied, but is not enough by itself. It is currently unknown how much precision the AGS operators will have running in the proposed MECO mode; this subject will be revisited when accelerator performance is better understood. Slicing the target along the length of the rod relieves axial stress; the effect this has on the Von Mises stress and, thus stability, is evident comparing Figure 11 with **Error! Reference source not found.**. While trial 10 of Table 4 has very low stress values, slices 0.1 cm thick and spaced 0.8 cm apart is complicated to construct and support because of the spread and curvature (due to the B-field) of the beam. Slotting at a fixed position along the length of each slice and axially can both further reduce stresses in the target; see **Error! Reference source not found.**.

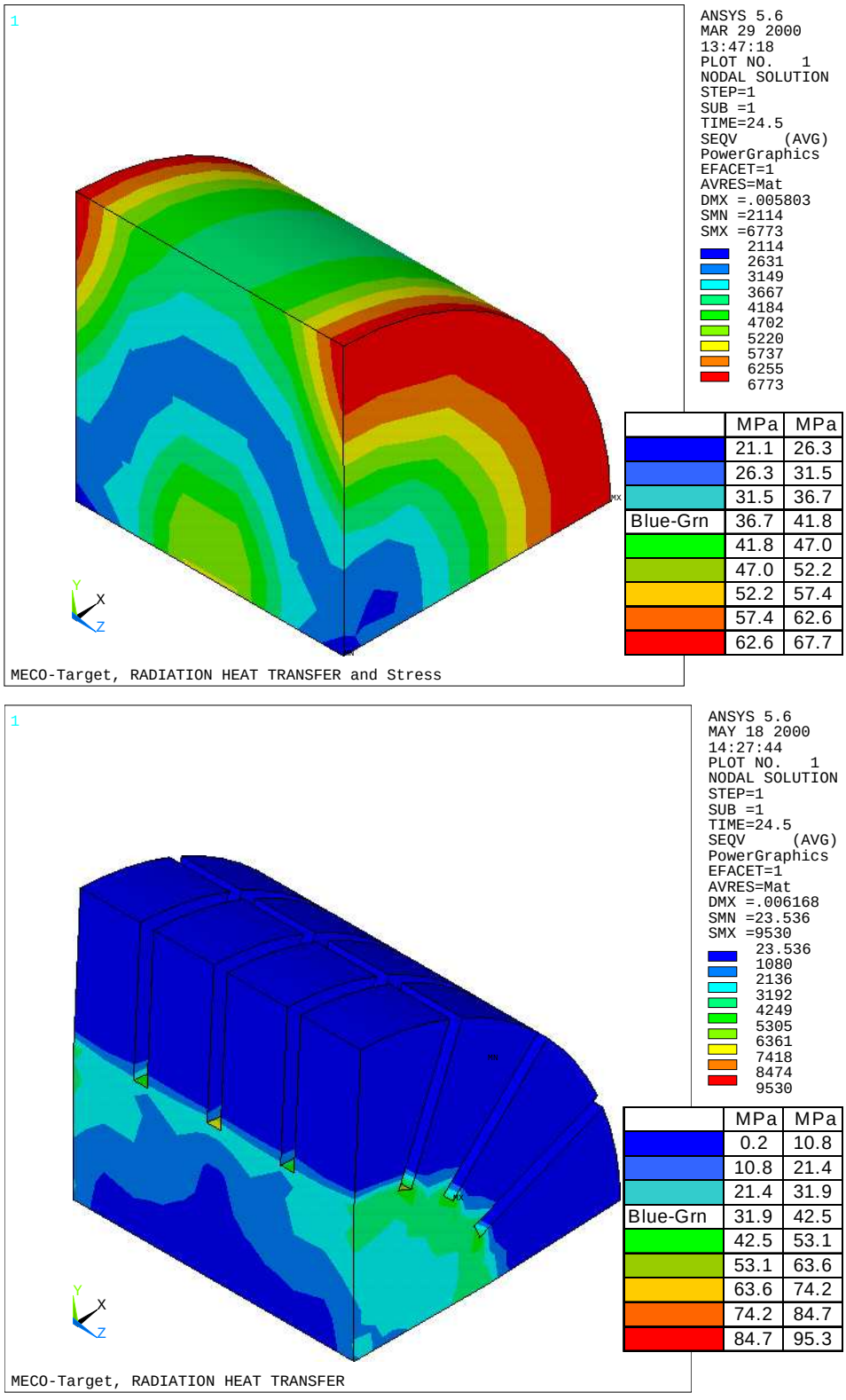

Figure 12: Local Von Mises stress distributions (N/cm^2) for a sliced target. A quarter of the slice at point of maximum energy deposition is shown. Length, 0.4 cm; radius, 0.4 cm; slice spacing, 0.8 cm. Trial 8 (top) and 10 (bottom) of Table 4.

1.5.2 Forced Convection

A water-cooled target has been designed using a high velocity water stream (turbulent) surrounding a cylindrical target in an annular coolant channel; see Figure 13. The coolant circulates in a closed loop, passing through a recouperative heat exchanger. A conceptual design of the full layout is shown in Figure 17. In this section, we will discuss the results of our design studies and prototype testing.

1.5.2.1 Cooling stytem overview

The current design, see Figure 13, calls for a gold or platinum rod, 16.0 cm long, with a 3.0 mm radius, and cooling channel gap size 0.3 mm. The coolant containment shell is made from a high-strength titanium alloy; it consists of five pieces: a cylindrical shell, two endcaps, and inlet & outlet pipes. The wall thickness of the cylindrical shell is 0.51 mm (0.020”) and the pipes have a 3.175 mm (0.125”) outer diameter, wall thickness 0.55 mm (0.021”), and 25 cm long. The endcap details appear in Figure 14. The target rod is held in position by three rounded feet at each end, shown in Figure 15, and forms the cooling channel.

.

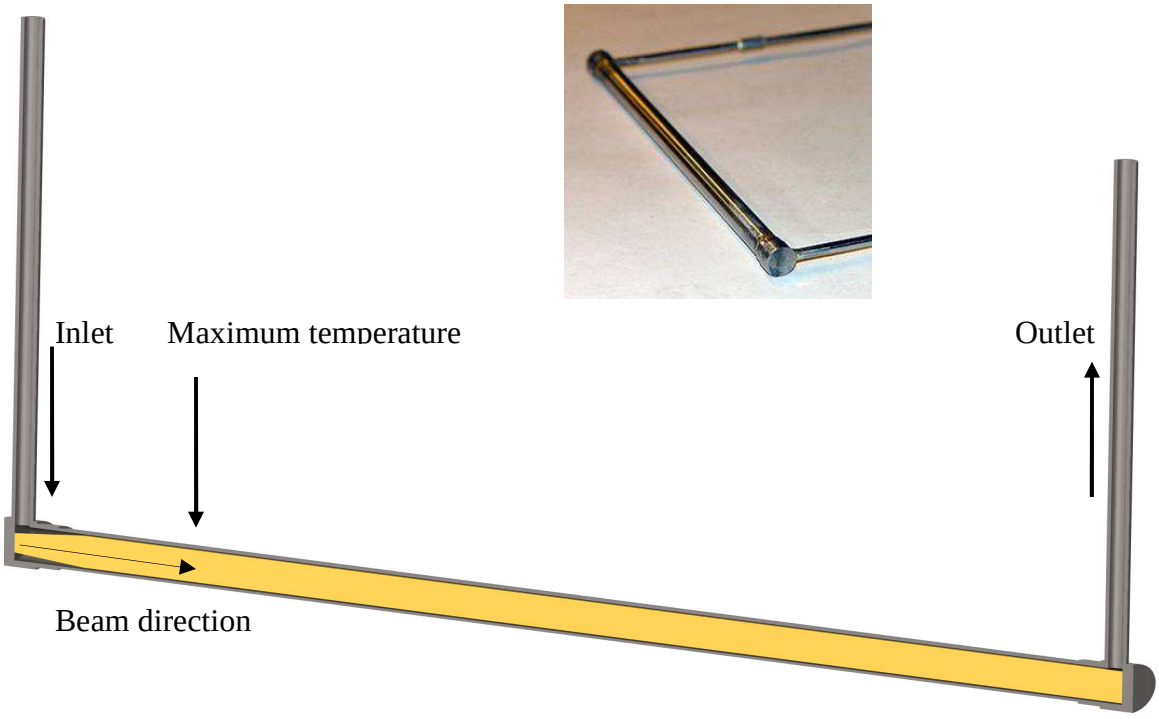

Figure 13: Cross-sectional view of current target cooling design. In our design, the beam strikes a gold target end-on from the left. The target shell, end caps, and inlet & outlet pipes are made of titanium. The target has a slight taper at the inlet which helps reduce the operating pressure; the coolant channel then narrows to 0.3 mm.

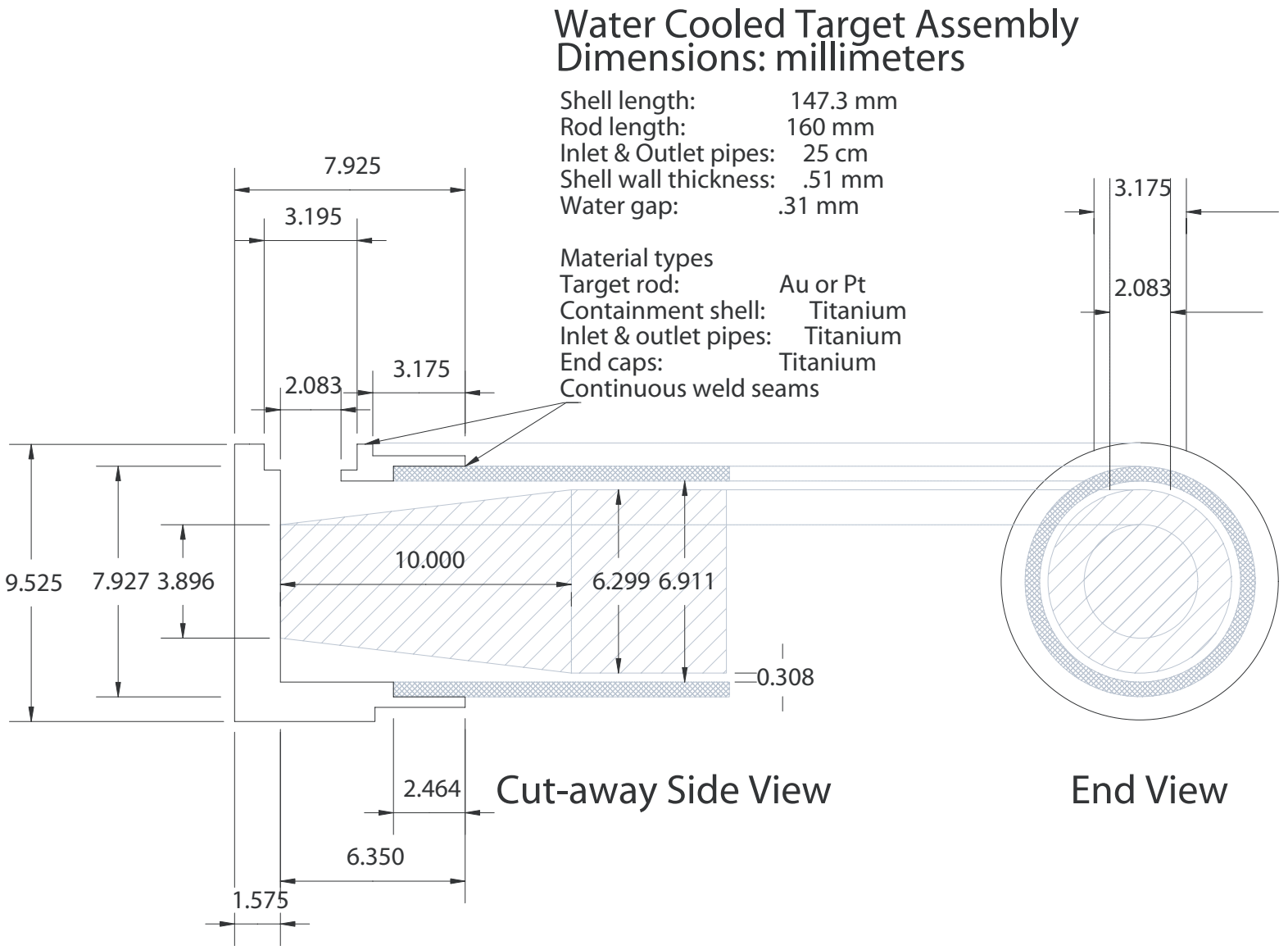

Figure 14: Endcap and inlet/outlet pipe design.

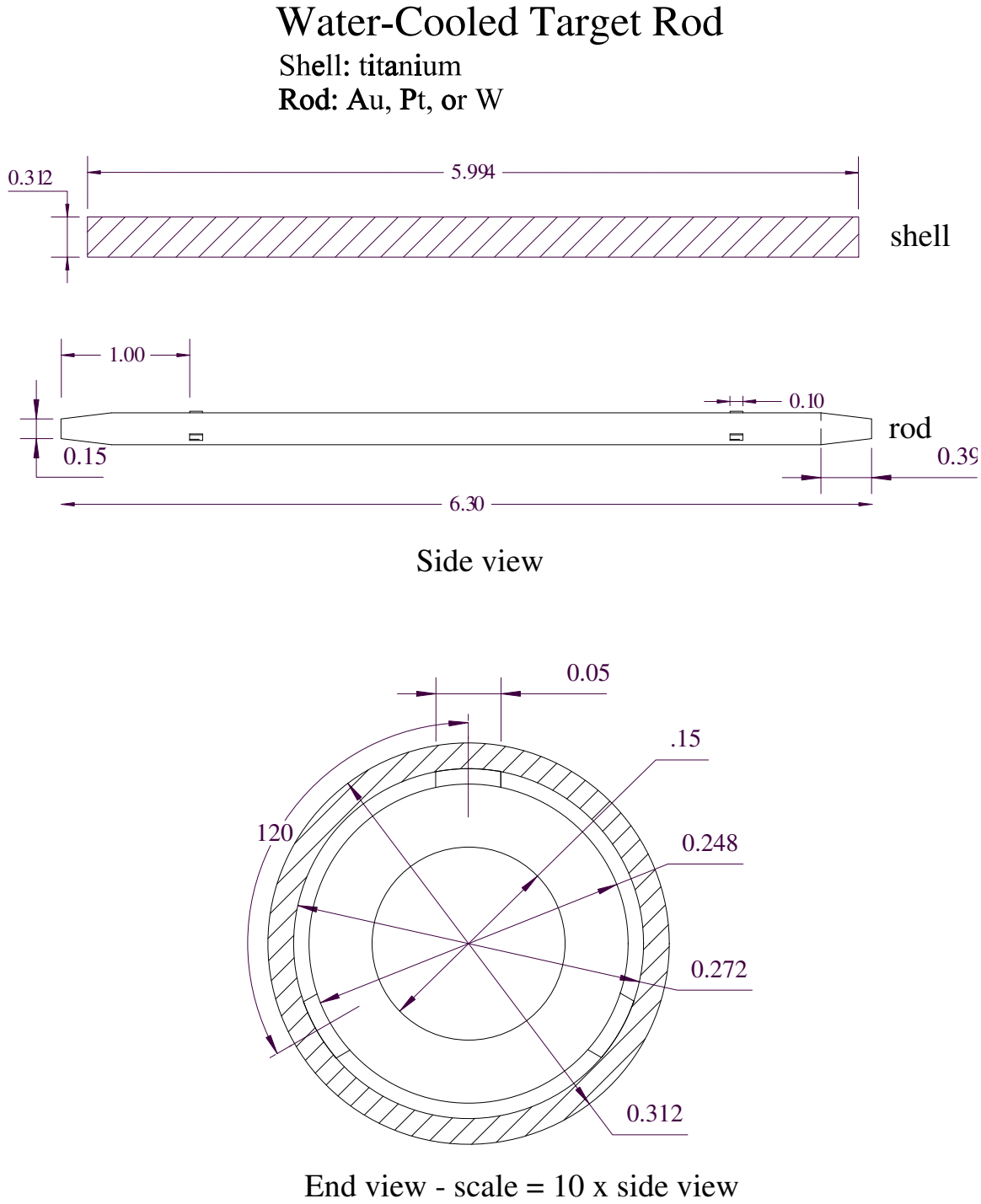

Figure 15: Target rod and shell design. Note that for the rod, current design calls for no tapered end at the outlet. The tube shaped "Shell" is constructed from high-strength titanium alloy. The "Rod" may be gold, tungsten, or platinum.

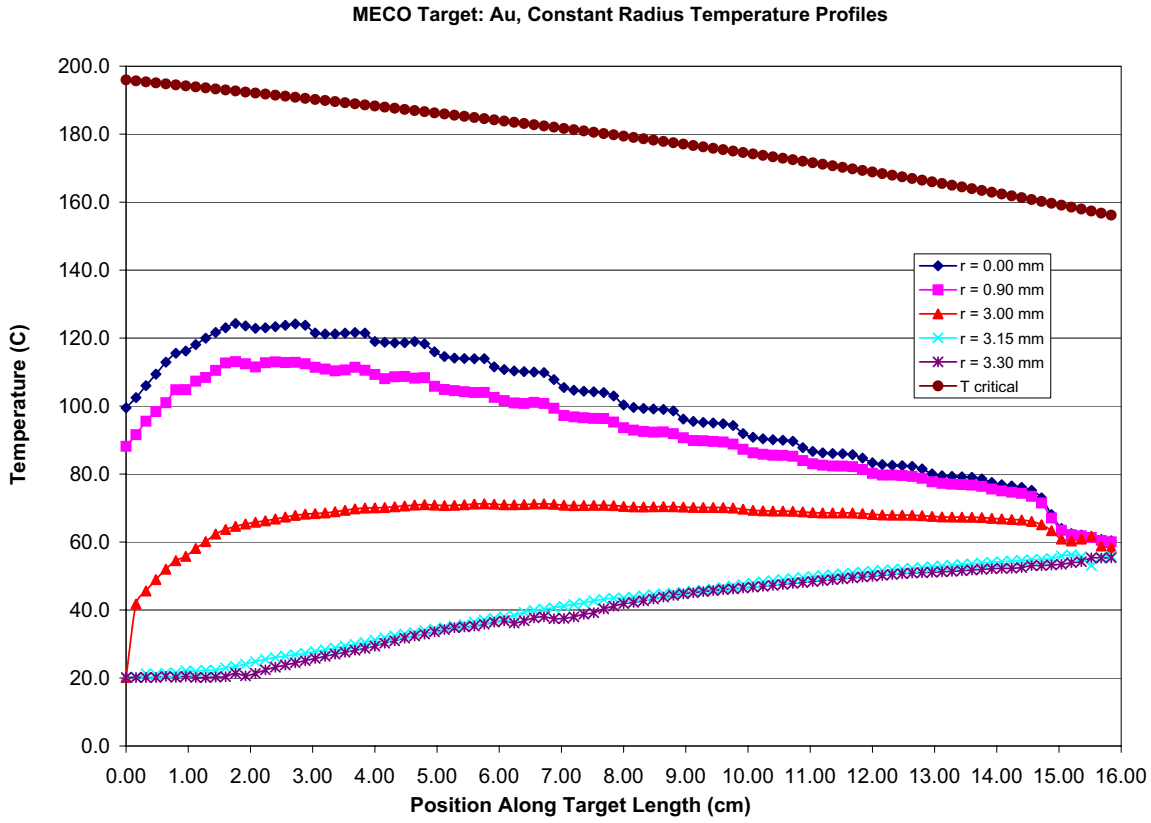

Figure 16: Target and coolant temperature at fixed radii as a function of position along the length. The results shown here are for a worst-case scenario, steady state heating, with power distribution shown in Figure 6 and 9500 Watts total instantaneous power.

Assuming an inlet water temperature 20 C and a volumetric flow rate of one gallon per minute, our calculations, shown in Figure 16, that the maximum target surface temperature (at the outlet) can be held at 71 C. Target surface temperature is given by the curve with r = 3.0 mm. The top curve, labeled $T_{critical}$, gives the boiling point assuming 25 cm inlet and outlet pipes

The conceptual design shown in Figure 17 conveys the general idea and we expect further development. The loop is designed to be a constant flow cooling system. There are three monitors for temperature; T_R (reservoir), T_{in} (inlet), and T_{out} (outlet), two for pressure, P_{in}, and P_{out}, and one volumetric flow sensor FM. The single-speed pump must provide a steady (non-pulsed) flow. There are many highly efficient, reliable, low flow impedance, compact recouperative (two separate fluid chambers) heat exchangers commercially available.[i]

Coordinated system control is essential. Flow is regulated with two needle valves, NV_1 and NV_2. The gate valves GV_1 through GV_4, and DV are necessary for servicing. All valves should be watertight, durable (e.g., stainless steel), with position indicators, and manual & remote control. All valves, the pump, and heat exchanger cold side supply should be mechanically slaved together to ensure they are operated properly; more importantly, the entire system must have electronic control and monitoring interlocked with the AGS. All sensors and hardware, except the titanium assembly, will be located far from radiation and magnetic fields; thus everything "above" GV_3 and GV_4, including these valves, will reside away from the PS.

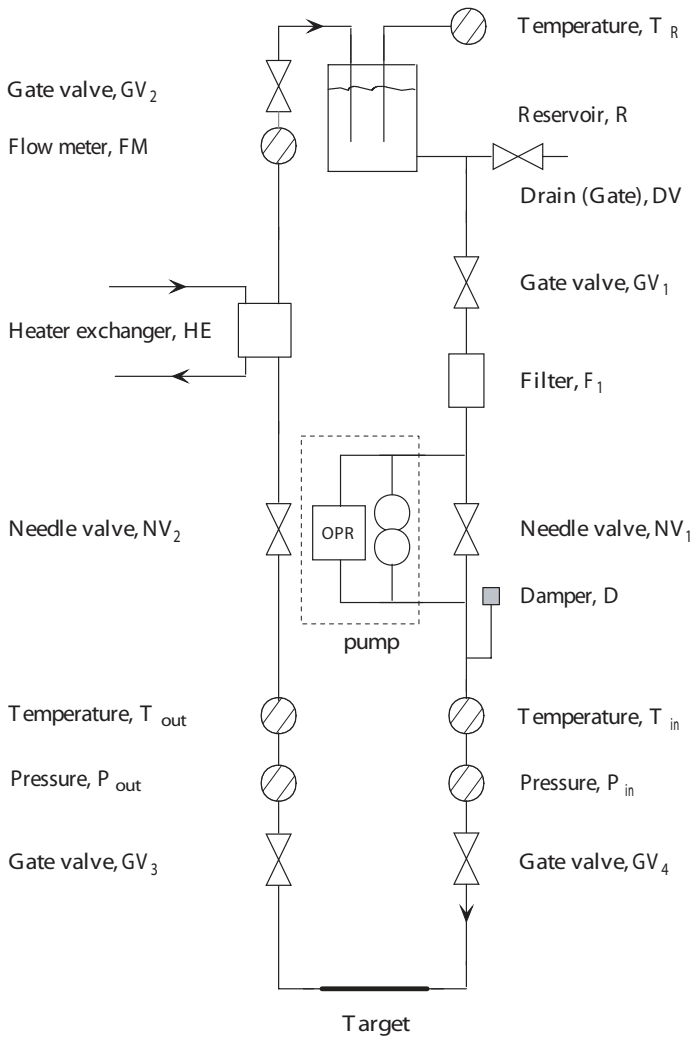

Figure 17: Conceptual design of the recirculating water-cooled target system for MECO. Note the over-pressure relief valve across the pump.

Construction and materials for coolant transport must be selected to maintain control over coolant leakage. Corrosion resistence, strength, radiation shielding must guide material selection. Figure 1 shows 0.5-inch titanium alloy service pipes connecting to the inlet and outlet pipes. These larger pipes extend out through the Production Solenoid vacuum bulkhead; see Figure 18 and Figure 19. A robotic arm will allow remote manipulate the entire titanium titanium assembly. The water pipes that connect to the target assembly and extend to the pump (to complete the circulation path) should be made of corrosion resistant high-strength stainless steel. According to Figure 18 the target-circulation system distance is approximately 40 feet; thus, the entire system should utilize 80-90 feet of stainless steel pipe. Although schedual 80 pipes were used in the test stand setup, proper wall thickness should be evaluated when coolant chemistry (along with other factors) is better understood. In any case, during target installation and removal, the two titanium and two steel pipes must be capped until connection is made. All joints, possibly with the exception of the connection just mentioned, should be welded continuously to ensure proper seals.

The amount and types of radioactive materials and chemical compounds that are formed in the coolant affect the size and composition of the reservoir R; the reservoir may also require a level indicator, as a safety precaution. Laboratory safety guidelines will determine the number of allowable Curies at a specified distance from the tank, and thus its design. Shielding may be required. Filtration needs are determined by the same coolant contamination factors mentioned above. A more appropriate filter location may be necessary.

Direct target temperature monitoring is unnecessary and posses no additional risk in operation; it is also advisable due to possible risks to pion reabsorption. At constant flow, water pressure and temperature monitors will serve as sensitive indicators of the state of the target. For example, a gradual accumulation of material in the flow channels would also cause an instant response and similar rise in pressure on P_{in}. Any narrowing of the cooling channel would produce a greater coolant velocity, thus raising the target cooling efficiency. A rise in target surface temperature will result in an instant rise in $T_{out.}$ Of course, a complete risk assessment of the cooling system will be required, and valid concerns addressed before a design is finalized.

The reliability of the system shown in Figure 17 has been extensively tested. We have built a mobile target test system, based on this design (with small practical modifications), which we have used to test full-scale target and cooling assembly prototypes, with and without heating. Target heating was done using induction heating with a radio frequency 20-kWatt power supply. All target testing results presented here were performed with the equipment described here.

Mechanical stresses in target assembly joints and components are very unlikely to reach dangerous levels. We recommend, based on our experience assembling numerous target prototypes, that joints be electron beam welded, to avoid damaging or distorting the flow channels. Compared to the importance of proper & continuous welding of all joints, individual component failure is remote. We have computed and verified the internal pressures likely to be present in the full-scale coolant recirculating system; these results are discussed below.

Surface roughness changes over time as coolant impurities attack (interact chemically with) the target surface. Impurities arise from target, coolant, and containment assembly materials undergoing nuclear fragmentation when they are in direct contact with the proton beam. This subject has not been fully explored yet.

The material that collects in the coolant and its concentration determine how it will be handled and stored. Tritium has a half-life of 12.3 years, making it one subject of possible concern. A cursory study of ^{3}H production using GEANT3 [11] showed that over the planned running time 4.72E-6 moles of tritium stop in the coolant that lies within the heat shield. Less than 1% of all tritium is produced by beam interactions in the water itself. The primary origin of tritium is due to beam particles interacting with the target. Tritium that stops in the coolant comes, primarily, from beam-induced nuclear fragmentation at the target surface; in fact, other elements in the cooling water also originate this way. When tritium comes in contact with oxygen it will form tritiated water, that is, one of the hydrogens in a water molecule is replaced by ^{3}H. Tritium can also form if suitably slow neutrons are present, by interacting directly with H or with ^{3}He. If we leave aside, for now, the neutron spectrum in the Production Solenoid region, the total tritium produced is small enough (based on [11]) that the tritiated water concentration will not reach a maximum. However, a mixture of tritium and water will result in some hydrogen gas production, as well as ^{3}He (decay product, but not a health hazard). There is also no danger present from hydrogen, since the concentration in air must rise above 4% before it is an

explosive risk. The low-energy electron, < 18.6 keV, from ^{3}H decay can be easily shielded. We plan to carry a complete study of coolant radiochemistry to understand what hazards exist and how to prevent them.

MECO Final Installation

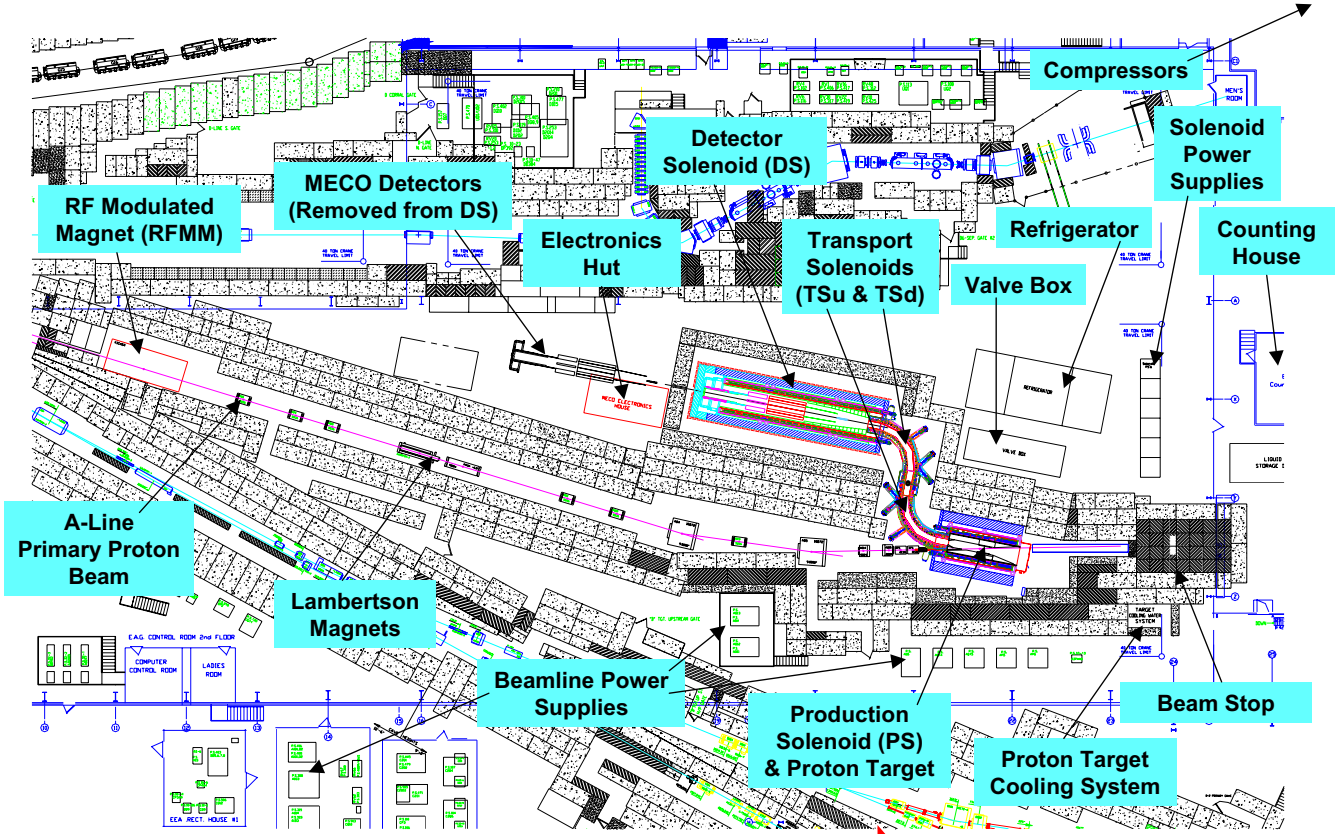

Figure 18: Layout of MECO final installation. The Prodution Target and Cooling System locations are clearly marked with red stars. Viewed while reading this caption, the cooling system is at the bottom left of the figure, just next to the AGS Beam Stop.

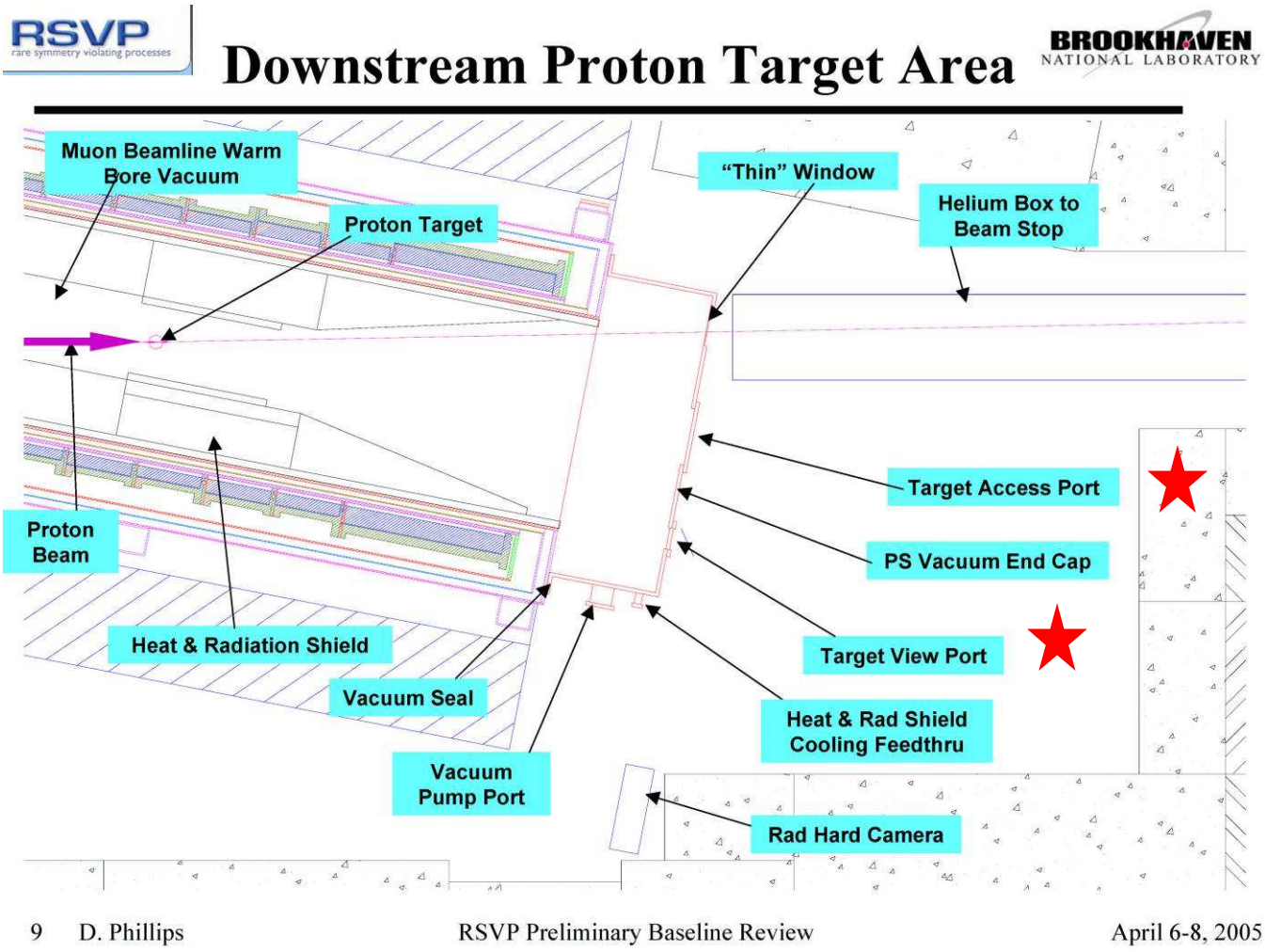

Figure 19: Downstream production target area. Note the target access port and view port are indicated with red stars.

1.5.2.2 Cooling design calculations

The flow conditions in the MECO target are necessarily turbulent. That is, there is a mean (time averaged) flow velocity at every location in the fluid; but the overall flow is unstable, due to persistent fluctuations locally in space and time in fluid element motion, boundaries, and thermodynamic conditions. Closer to the surfaces of the water containment channels the fluctuations cease and the fluid slows to laminar flow; continuing to the walls a real (finite viscosity) fluid must come to rest.

Our chief calculation tool has been CFDesign, a heat and mass transfer program designed for solving complex engineering problems. In all calculations, we have tried to assume "worse case" conditions. Thus, the water containment shell is assumed to be an adiabatic wall - ensuring all heat transfer takes place in the rod and water, the instantaneous power delivered to the rod is 9500 Watts, and is continuous (not pulsed). The fact that the actual inlet to the water jacket is perpendicular to the rod has a modest effect on flow, pressure, and temperature in practice, as we shall see. So, for simplicity, we choose the boundary condition of a uniform inlet flow velocity parallel to the rod. Our calculations included the temperature dependence of all relavant physical properties: viscosity, specific heat, and thermal conductivity.

CFDesign has many features that speed the process along. One, in particular, is a great aid in getting started: the software generates a mesh in the space one wishes to study heat and mass transfer; using various algorithms to determine how many mesh points are required and their distribution based on the given the boundary conditions, geometry, and desired precision. However, one must always vary precision and conditions about their desired values to assess the stability of the numerical solution. Hence, multiple calculations are sometimes unavoidable. Figure 21 illustrates how we setup our calculations: rotational symmetry (if feet are neglected) reduces the problem to two spatial variables, the coordinate directions are drawn, we have labeled each surface, and the left end is the channel inlet.

Error! Reference source not found. and Figure 24 show the time averaged temperature profile (cylindrical coordinates, r and z) of a gold target without tapered ends. The maximum core temperature is lowest for gold, due its high thermal conductivity; in this case we have a maximum temperature of 397.6 K (124.6 C). Away from the containment wall, the bulk motion of the water dominates heat transfer in the fluid; however, on a scale of tens of microns above the target surface, the fluid moves very slowly and heat transfer here is diffusion dominated and thus limited by the thermal conductivity of the water. The target surface temperature is 350 K (77 C).

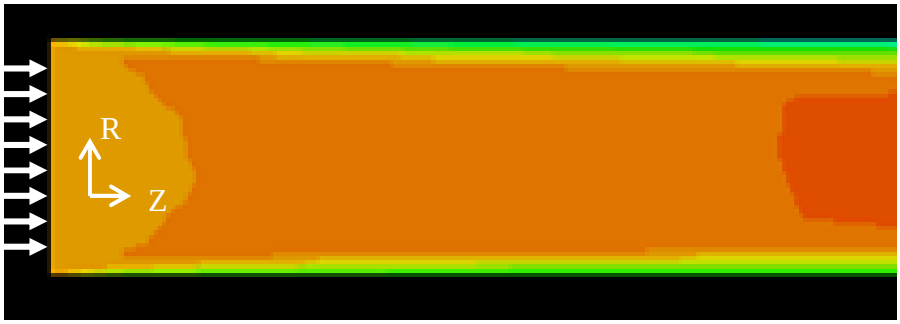

Figure 20: All design calculations assume a uniform fluid velocity at the inlet.

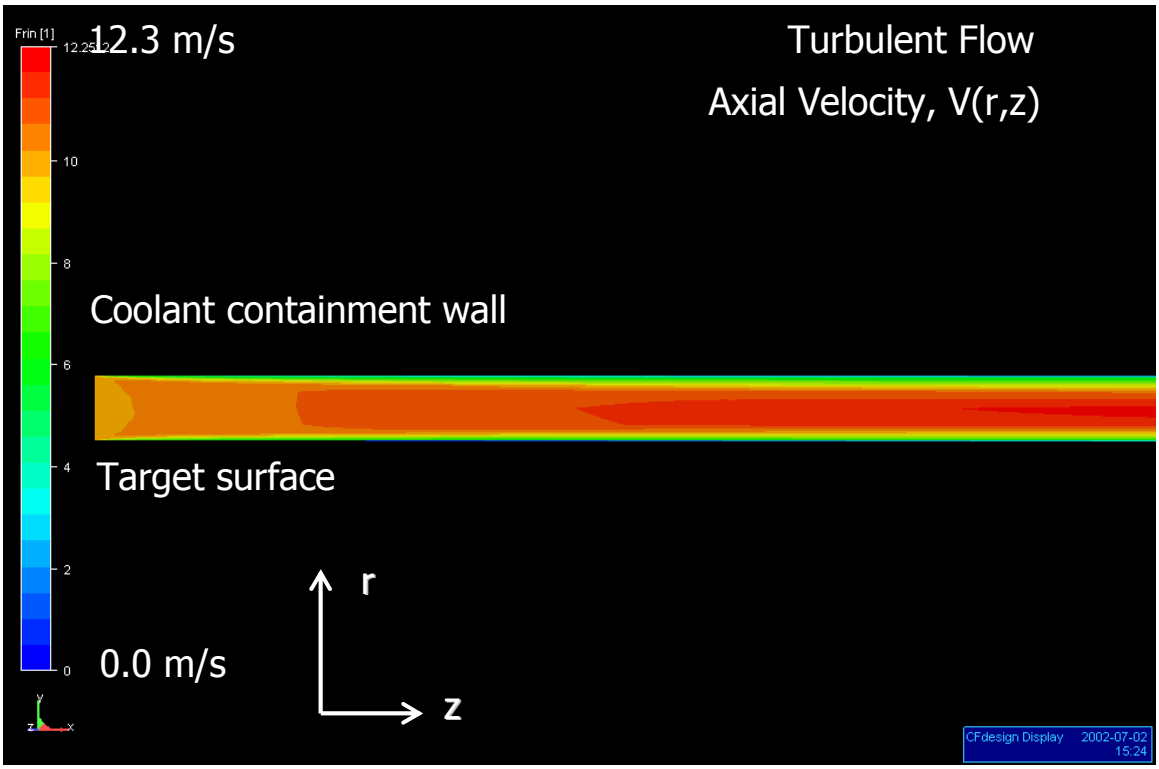

Figure 21: Axial fluid velocity profile illustrating the general layout of the calculations.

Error! Reference source not found. and Figure 24 show the time averaged temperature profile (cylindrical coordinates, r and z) of a gold target without tapered ends. The maximum core temperature is lowest for gold, due its high thermal conductivity; in this case we have a maximum temperature of 397.6 K (124.6 C). Away from the containment wall, the bulk motion of the water dominates heat transfer in the fluid; however, on a scale of tens of microns above the target surface, the fluid moves very slowly and heat transfer here is diffusion dominated and thus limited by the thermal conductivity of the water. The target surface temperature is 350 K (77 C).

Good heat distribution in the coolant, particularly over the energy deposition maximum, means that we must attain a turbulent condition as soon as possible after a fluid element enters the gap. In circular ducts the transition from stable laminar flow to fully developed turbulent flow occurs over the range of Reynolds numbers Re: 2100-4000. The maximum water flow velocity in the MECO target is above 10.5 m/s, leading to a local value of Re: 12000-24500. Our calculations suggest that fully developed turbulence is attained in about 7 gap thicknesses, which is certainly adequate.

The importance of minimizing mass in the inner bore of the Production Solenoid makes it desirable to have the water containment assembly as thin as possible; however, restraining internal pressure drives the design to minimize the ratio of radius to wall thickness of the weakest component, the cylindrical shell. Our calculations suggest that at one gallon per minute the pressure drop from inlet to outlet is below 150 psi, a fact confirmed in flow test results (prototype 03) shown in Figure 31; see Figure 13 through Figure 15 for target details. A slight taper in the rod was introduced at the inlet to reduce the pressure drop to about 110 psi. Measurements at the above flow rate show that the pressure drop across each pipe is 67 psi.

The maximum gauge pressure at any point in the system outlined in Figure 17 is expected to be below 250 psi. The half-inch titanium alloy service pipes will extend out of the high radiation and magnetic field region connect to stainless steel pipes extending behind the iron return yoke, away from the high radiation and magnetic field region between the upstream end of the muon beamline and the beamdump. and heat exchanger constribute less than 1-2 atmospheres are unlikely to raise the pressure drop across the recirculating pump by an amount comparable to that across the assembly, the actual operating pressure at every point in the target assembly when installed inside the Production Solenoid is likely to be below approximately 300 psi. Our calculations indicate that tensile stresses in the water containment assembly are no more than a factor 10 higher than the maximum pressure. Thus, since the tensile yield stress of high-strength titanium alloys is typically between 100,000-200,000 psi, the system we designed will operate at stresses at least one-tenth the elastic limit of the construction material.

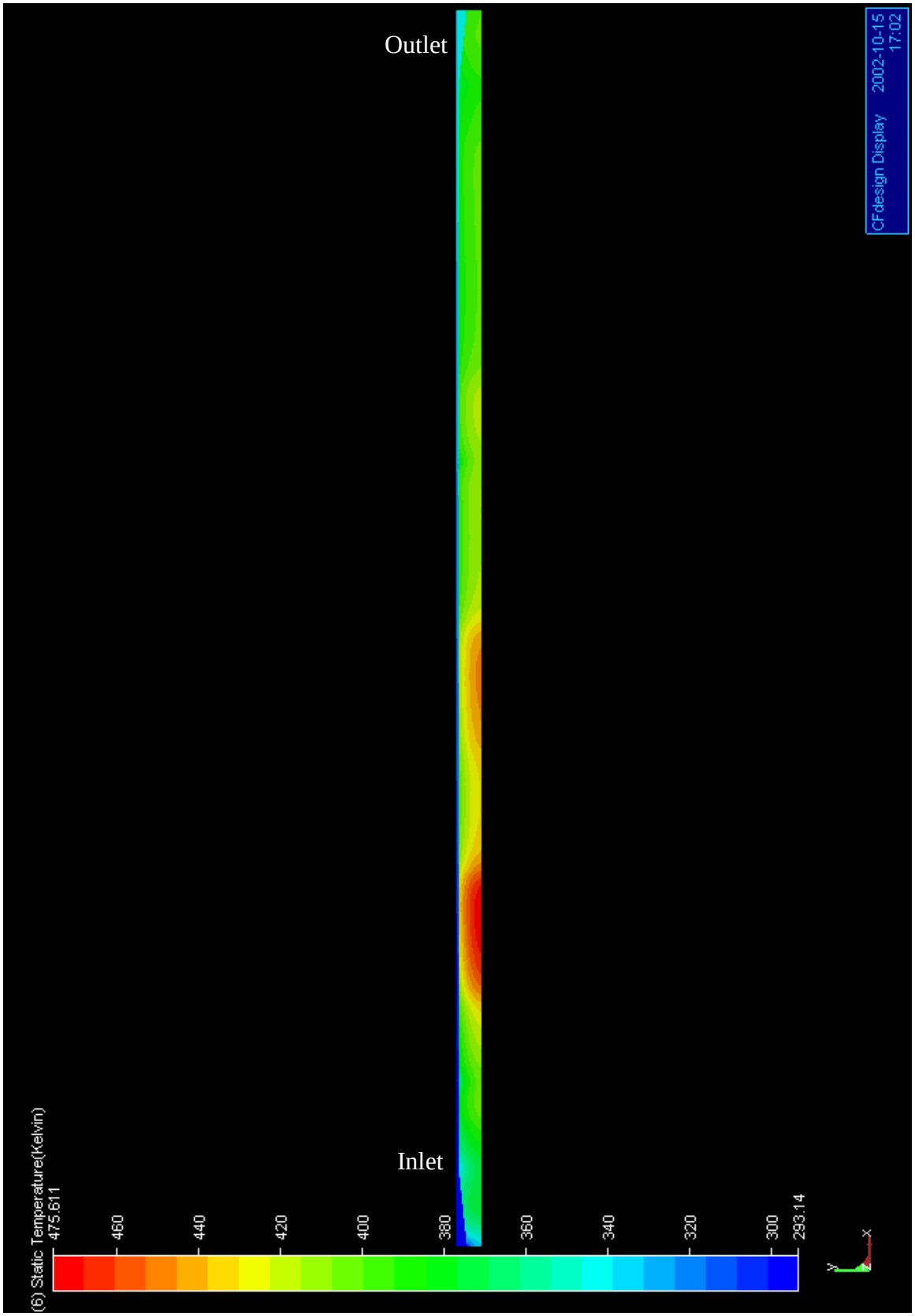

Figure 22: Temperature (K) profile for prototype 03, target with tapered inlet, water channel, and straight outlet.

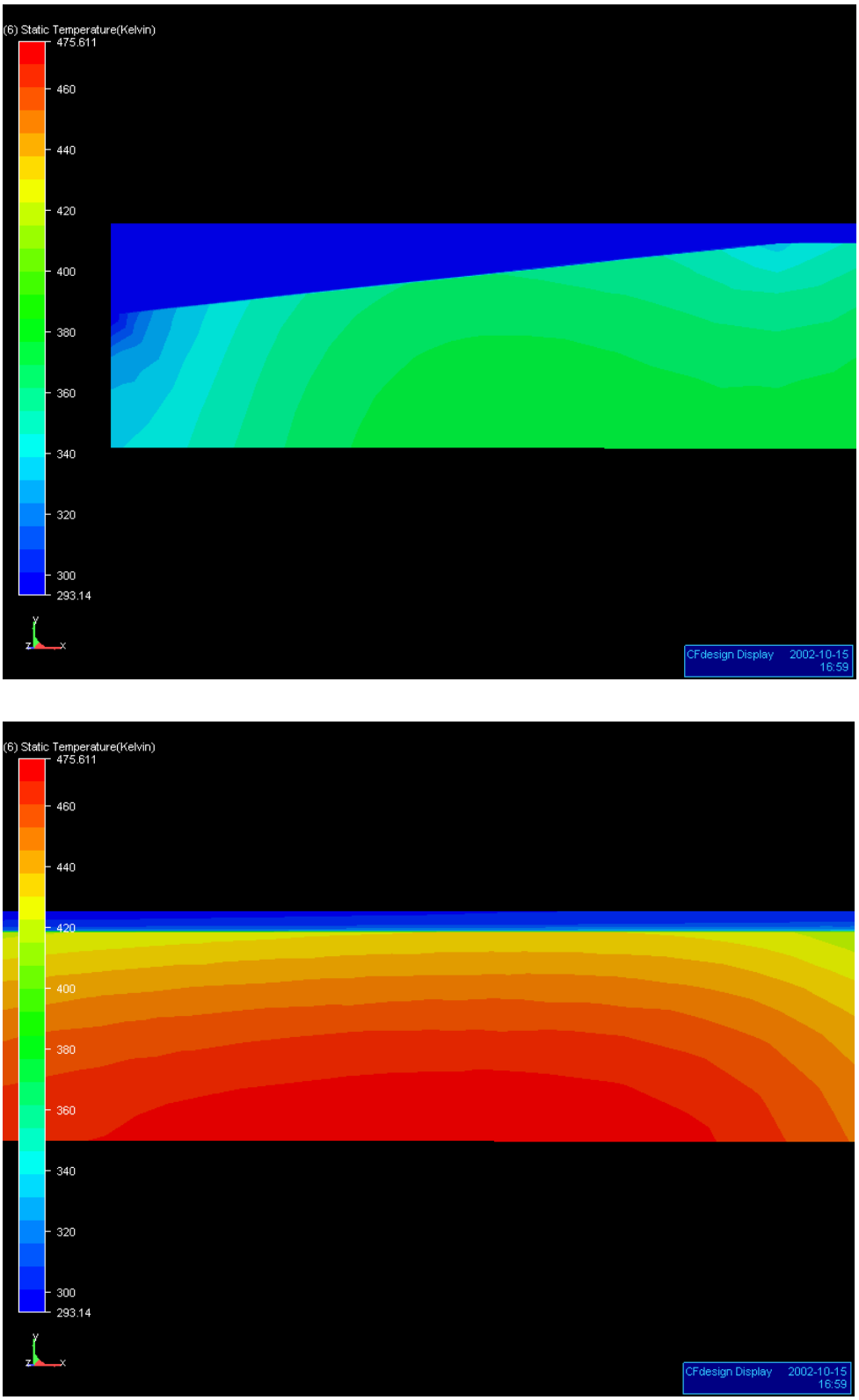

Figure 23: Prototype 03 temperature distribution (K), close-up of inlet (top) and water channel-target interface over the location of maximum energy deposition (bottom). Conditions: target radius 3.0 mm, radius 0.3 mm, 1 gpm.

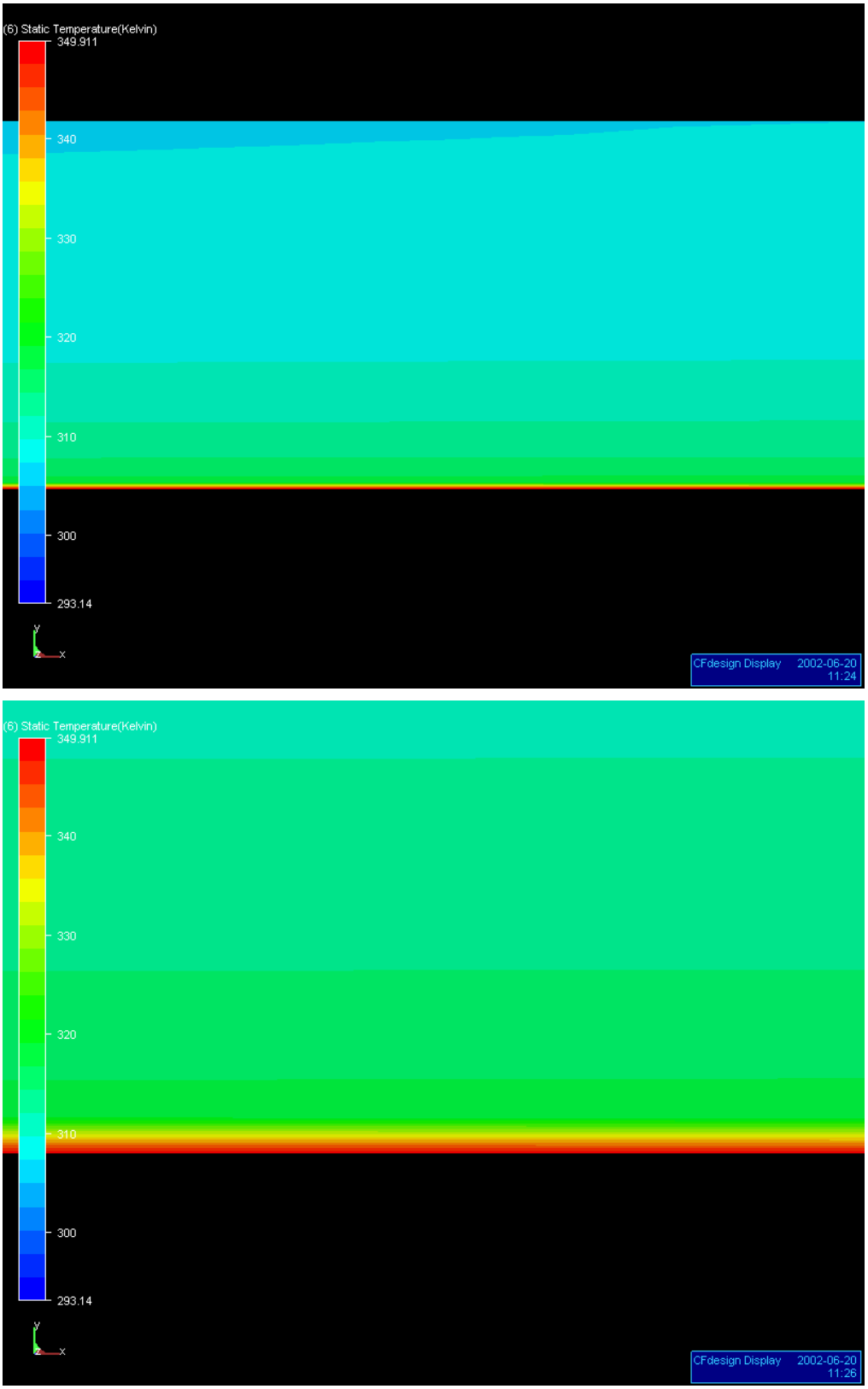

Figure 24: Magnification of coolant channel temperature distribution, revealing the thin diffusion dominated heat transfer layer: 10-20 microns. Target surface temperature is 350 K (77 C). Conditions: 1 gpm, target radius 3.0 mm, gap 0.3 mm, uniform heat flux through target surface – total 9500 Watts.

1.5.2.3 Target testing system

To confirm our target design calculations and test our coolant circulation & heat management system design a unit was built to test target prototypes; see Figure 25. Our tests proceeded in two stages: optimizing flow vs. pressure drop and then cooling tests. Six prototype designs have been tested; efforts were aimed at optimizing target geometry with regard to flow, pressure, and cooling, assembly methods, and the design of the coolant containment shell for heating tests. Roadmap!

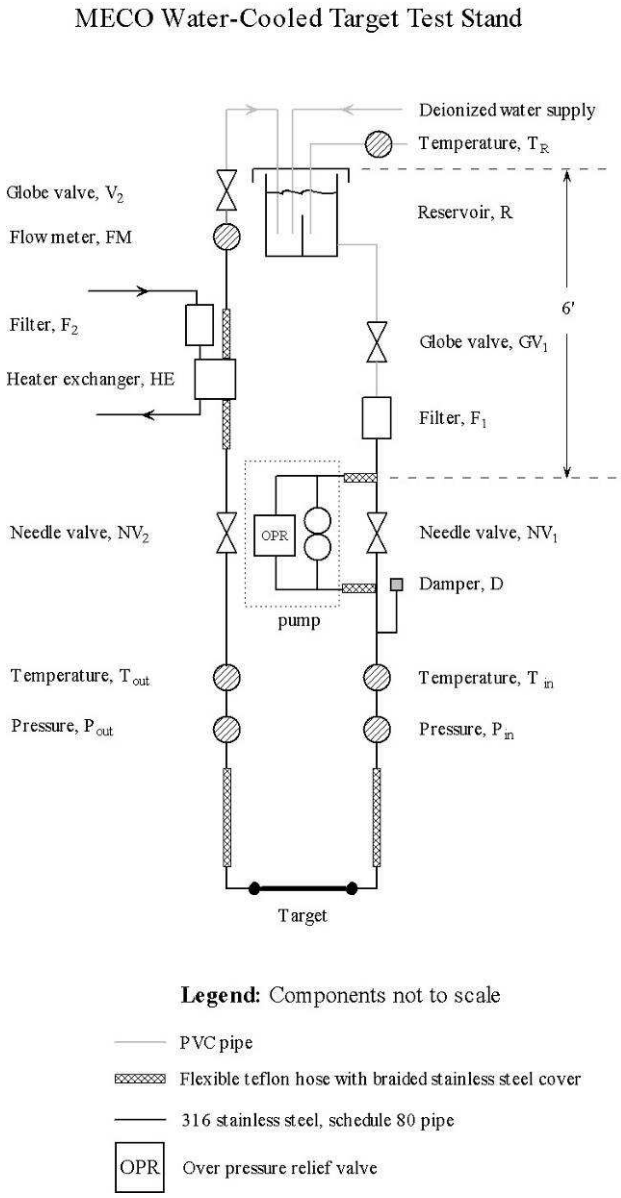

Figure 25: Mobil target test stand. Thermistors and thermocouples proved to be useful as temperature monitors. Pressure sensors proved durable and reliable, with 0-300 psi, less than 1% accuracy full scale, superior linearity, excellent repeatability, 0-30 Volts DC output, and good shielding. The flow sensor, of the impeller type, with 0-6 V output. Flow rate and frequency were linear to better than 1% over 0.1–10 gpm; pressure drop across the unit was no more than 1-2 psi at 1 gpm. The rotary vane pump[ii] produced no measurable flow pulsing. A circulation pumpwas placed in the reservoir to maintain a homogeneous temperature (not shown).

Test stand flow control is very simple. While filling the reservoir R, valves GV_1 and GV_2 are closed, and then opened after the deionized (preferably distilled) water suppy is shut off. Beginning with the pump off, NV_2 is closed and NV_1 is open. The pump is switched on, circulating the water through NV_1 and back through the pump. Clearly, at this point the flow meter FM reads zero flow. The desired flow range is obtained as follows. The pressure at P_{in} and P_{out} must read the same, as they are shown to be in Figure 26. As NV_2 is opened, P_{out} falls. When NV_2 is completely open, P_{out} is only a few psi above atmospheric pressure. The discontinuity in the slope at approximately 0.6 gpm marks the beginning of the process of closing NV_1.

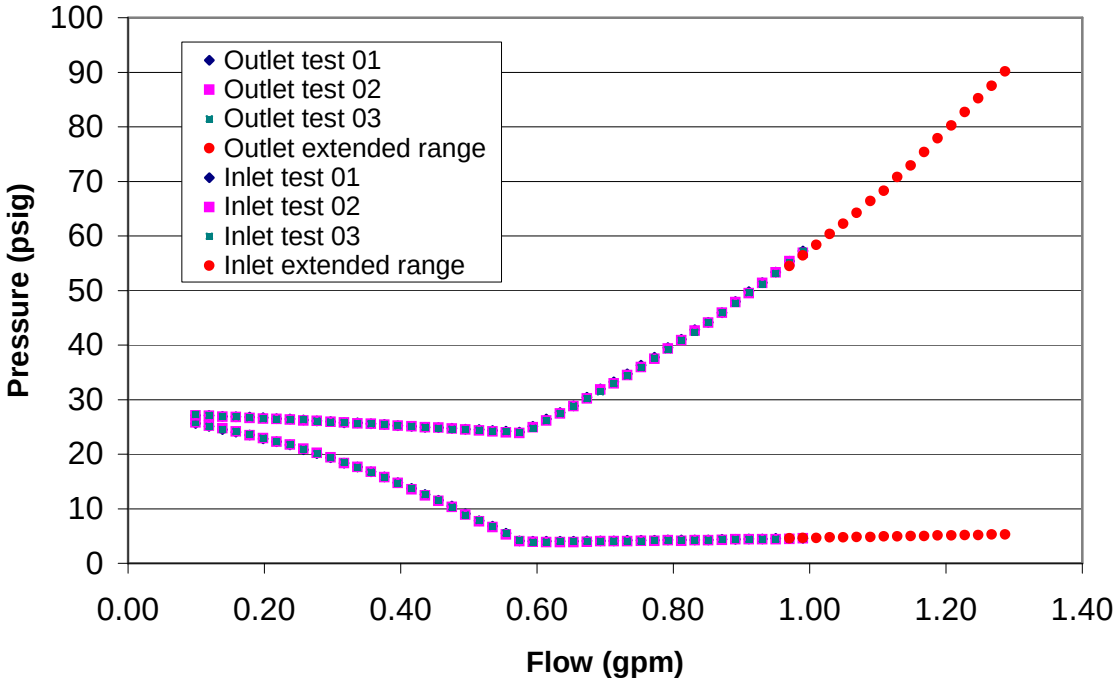

Figure 26: Test stand operation and repeatability. The target is unspecified here, however the qualitative features of the curves remain the same regardless of the target design. The lower curve corresponds to NV_2 (P_{out}) and the upper to NV_1 (P_{in}). The lower limit of the flow meter FM is approximately 0.1 gpm.

The heat exchanger chosen for the test stand, shown in Figure 27, is highly efficient, with a negligible pressure drop on each side. The hot side is expected to operate at 1 gpm and the cold at 6-12 gpm; thus, according to Figure 28 both sides experience relatively small pressure drop, hot side <1.0 psi. The heat transfer coefficient of the unit, using incompressible fluids, relates the heat flow to the difference in inlet temperatures:

$$P = \alpha(Q_{\text{hot}}, Q_{\text{cold}})(T_{\text{in}}^{\text{hot}} - T_{\text{in}}^{\text{cold}}),$$

where P has units of power, Q is volumetric flow rate, and T is temperature.The superscripts “hot” and “cold” refer to the side of the heat exchanger. The flow rates, gallons per minute, are designated as Q.

Figure 27: Lytron LL820G02: Counter-flow liquid-to-liquid 20 copper brazed plate heat exchanger.

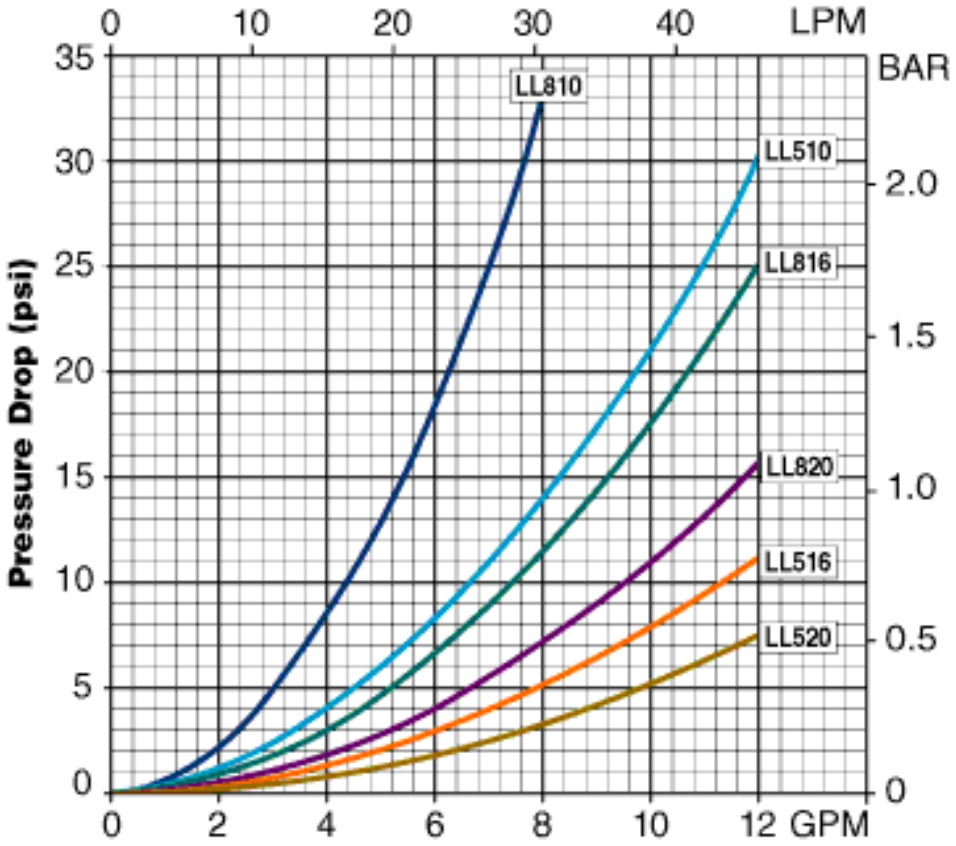

Figure 28: Heat exchanger pressure drop, Lytron LL820G02. The horizontal axis is the flow rate for either fluid side, in gallons per minute (gpm); gauge pressure is in pounds per squiare inch (psi).

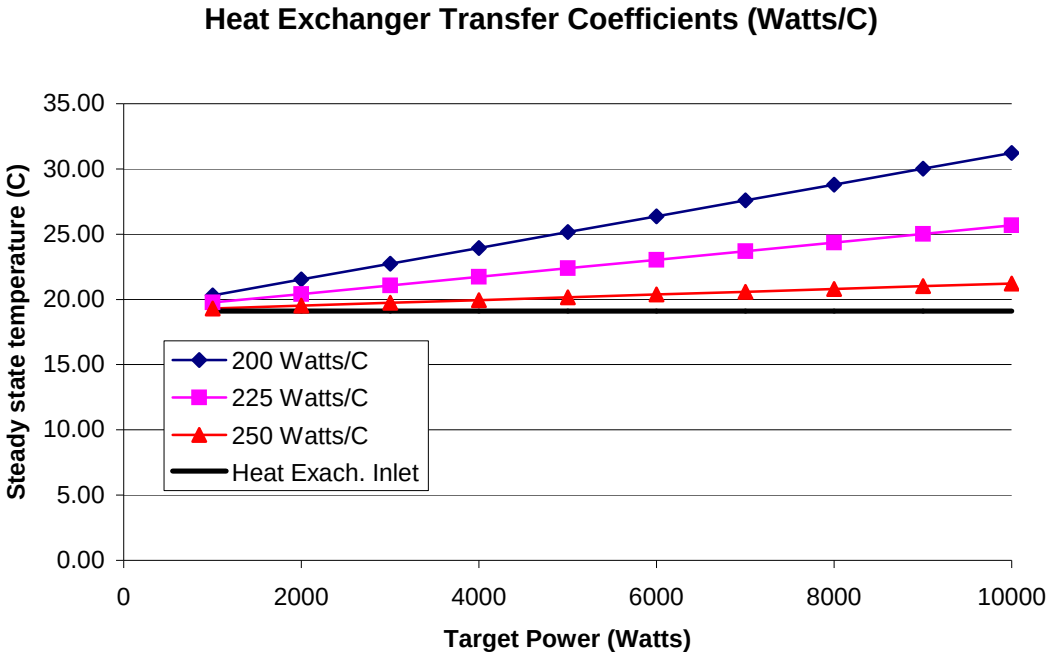
Heat Exchanger Transfer Coefficients (Watts/C)
Steady state temperature (C)
35.00
30.00
25.00
20.00
15.00
10.00
5.00
0.00
0
2000
4000
6000
8000
10000
Target Power (Watts)
200 Watts/C
225 Watts/C
250 Watts/C
Heat Exach. Inlet

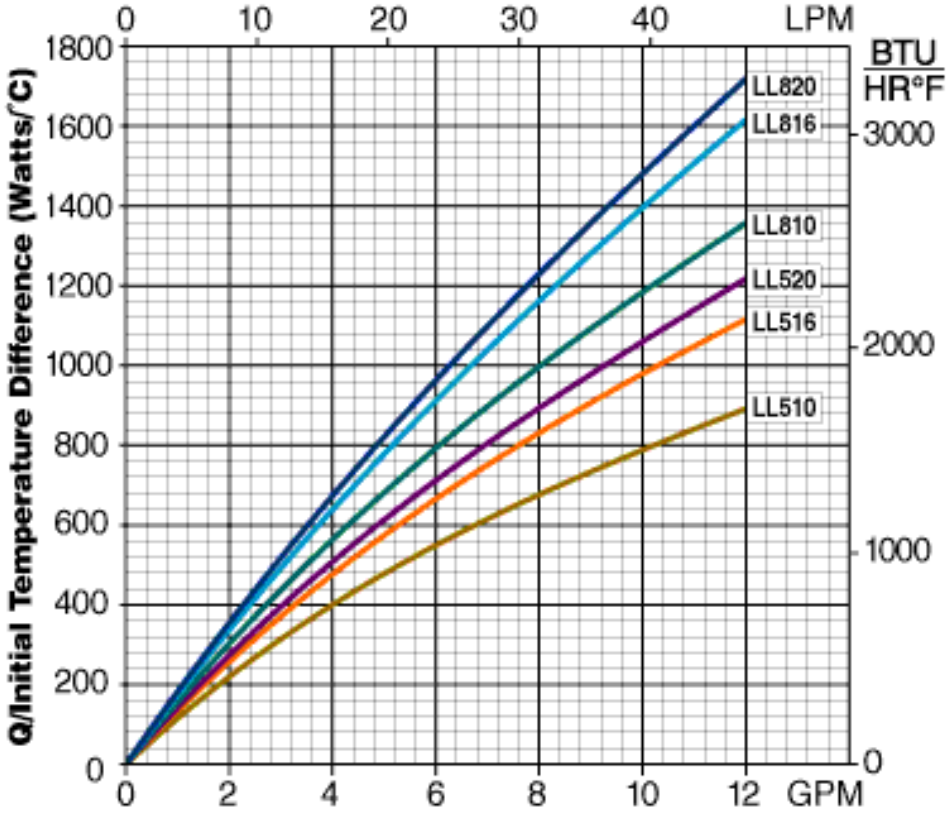
Q/Initial Temperature Difference (Watts/°C)
1800
1600
1400
1200
1000
800
600
400
200
0
0
10
20
30
40
LPM
0
2
4
6
8
10
12
GPM
BTU
HR°F
3000
2000
1000
0
LL820
LL816
LL810
LL520
LL516
LL510

1.5.2.4 Target flow tests

The first crucial series of tests was to optimize and characterize the volumetric flow vs. pressure relationship of the target geometry and coolant containment assembly. Prototype 03 has shown the best performance. Pressure is a quadratic function of flow, aas shown in Figure 31. At 1.0 gpm, the pressure drop across the target itself is 100 psi. A photograph of the full-scale prototype with inlet and outlet pipes, mounted for testing is shown in Figure 29.

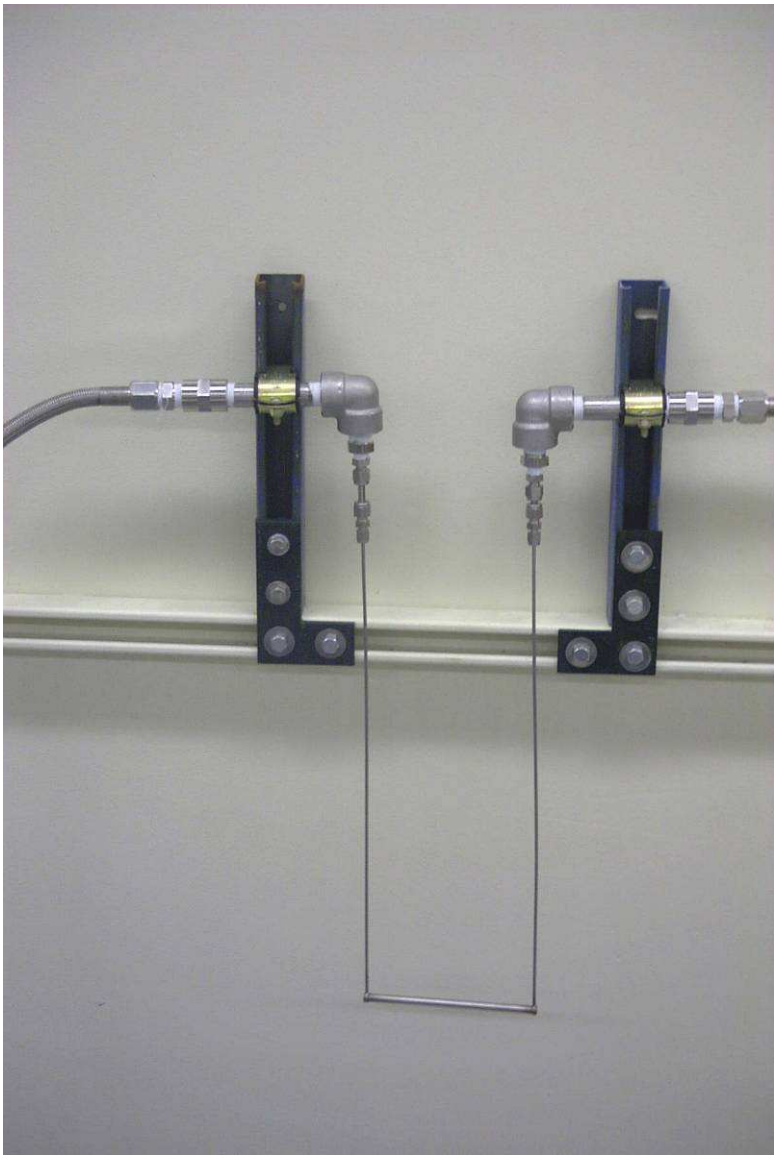

Figure 29: Photograph of full-scale prototype target, shell, end caps, and 30 cm long inlet/outlet pipes.

Target geometry must be able to accept the inlet stream with gradually changing surfaces that do not create dead zones and vortices; prototype 02, Figure 30, has both design flaws. Prototype 03, seen in Figure 14 and Figure 15, corrects this with a tapered inlet. Figure 31 compares our design calculations with experiment, which are in approximate agreement. One may also infer that inlet & outlet approximations and neglecting the three-dimensional nature of the target with "feet" were very helpful and time-saving simplifications.

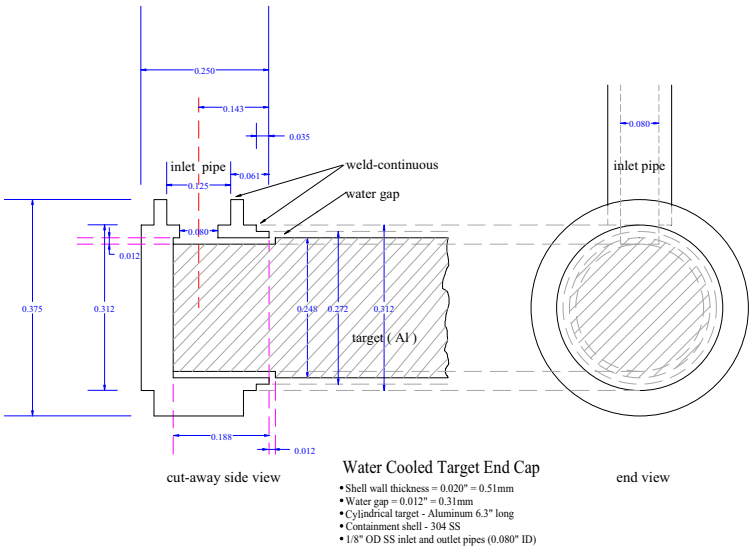

Figure 30: Target prototype 02. Target has right angle steps at both ends.

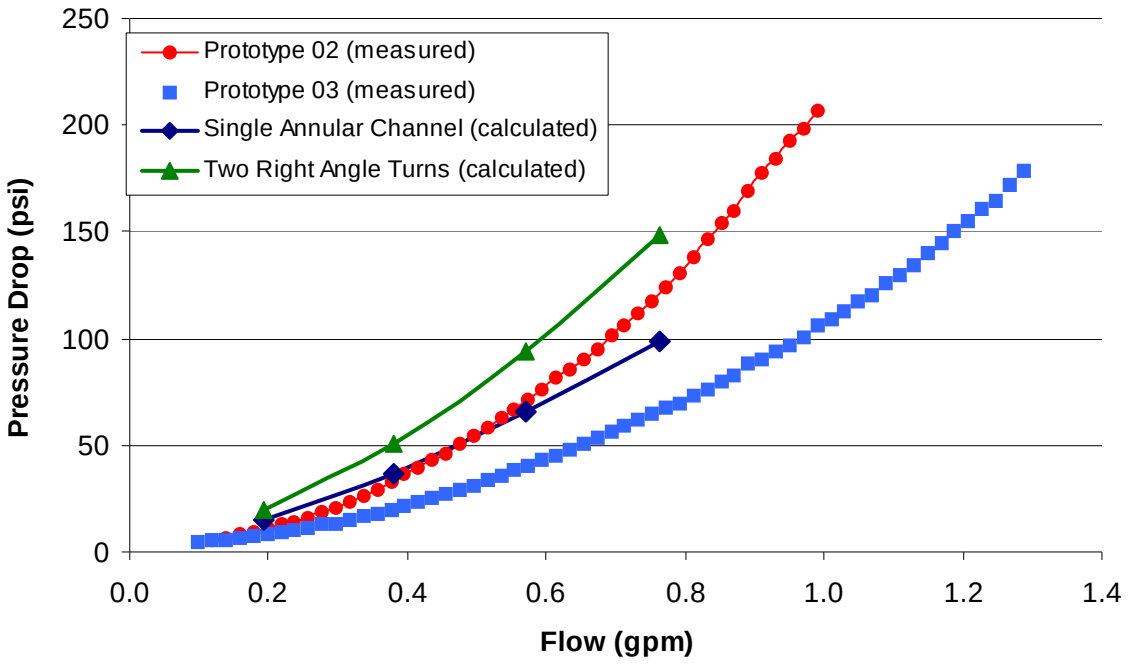

Figure 31: Comparison between two target geometries.

1.5.2.5 Target cooling tests

Target cooling tests were both a test of our coolant containment assembly and our monitoring system design. Flow rate controls pressure and temperature at all locations in the system; with the exception of the reservoir, at atmospheric pressure. The crucial quantities to measure are the power delivered to the target, the maximum target surface temperature, pressure drop across the target, absolute pressure, and how the system temperature reaches steady state. Independent confirmation of these quantities serves as a useful check during the experiment and adds to the repeatability of the measurements themselves; thus, as many sensors as was practical were positioned around the coolant circuit.

A high-frequency power supply [12] designed to heat treat metal components provides good control over target heating. Maximum power delivery to the work piece is obtained using as high a frequency as possible; the metal should be chosen to have minimum skin depth and the coil as many turns per unit length as possible. Figure 32 illustrates the basic components involved with induction heating. A hollow copper coil is wrapped around the work piece and connected to the power source. Water flows through the coil for cooling. When the AC power unit is activiated, an oscillating magnetic field generates eddy currents in the metal rod. The skin effect in metals confines the eddy currents to a region near the surface. The skin depth $\delta = \sqrt{2\rho/\omega\mu}$ sets the length scale of this region and depends on the resistivity ρ, angular frequency ω, and magnetic permeability μ. Assuming a long coil, the power per unit area delivered to the rod is $P/A_{\text{rod}} = \frac{\rho H_0^2}{2\delta} f(R_{\text{rod}}/\delta)$, with the surface area of the rod covered by the coil $A_{\text{rod}} = 2\pi R_{\text{rod}} \lambda_{\text{coil.}}$ The function of the ratio of rod radius to skin depth is an expression involving Bessel functions, which need not concern us now[13, 14]. The magnetic field of the coil is not uniform or simple; however, as for all solenoids, its size depends on the number of coil turns per unit length times the coil current.

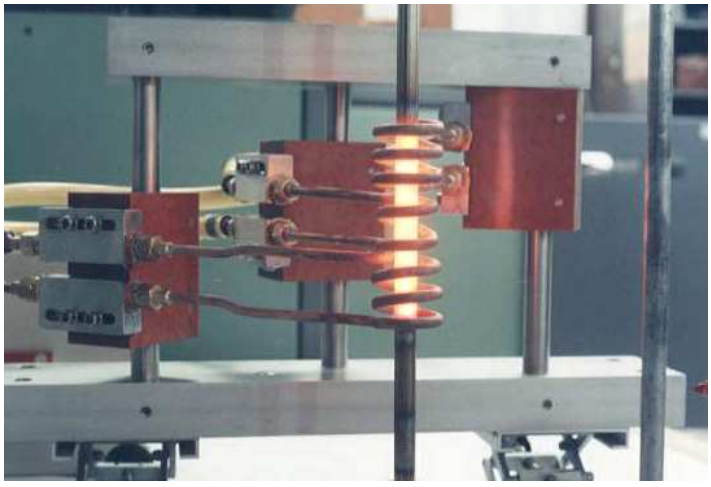

Figure 32: Example of induction heating. Note there are two separate coils in this picture.

Another important benefit of induction heating at high frequencies is that it greatly simplifies target surface temperature measurements. For a very small value of δ/R_{rod}, the temperature profile in radius is constant for most of the body of the target, except as on draws within a few skin depths of the surface (neglecting end effects). The height of the drop in temperature as the surface is approached falls as the ratio $\delta/R_{rod.}$ The frequency of the power supply was 175 kHz and the target material was selected to have a high permeability, $\mu/\mu_0 = 2050$, giving a skin depth at this frequency of 0.018 mm. Solving Maxwells equations to obtain the eddy current density for a long coil and rod, one can compute the power deposition distribution. The heat condution equation, when solved, yields the temperature distribution relative to the surface temperature. Figure 33 shows the result of our calculation. Indeed temperature varies very little inside the rod and temperature sensor positioning is not crucial.

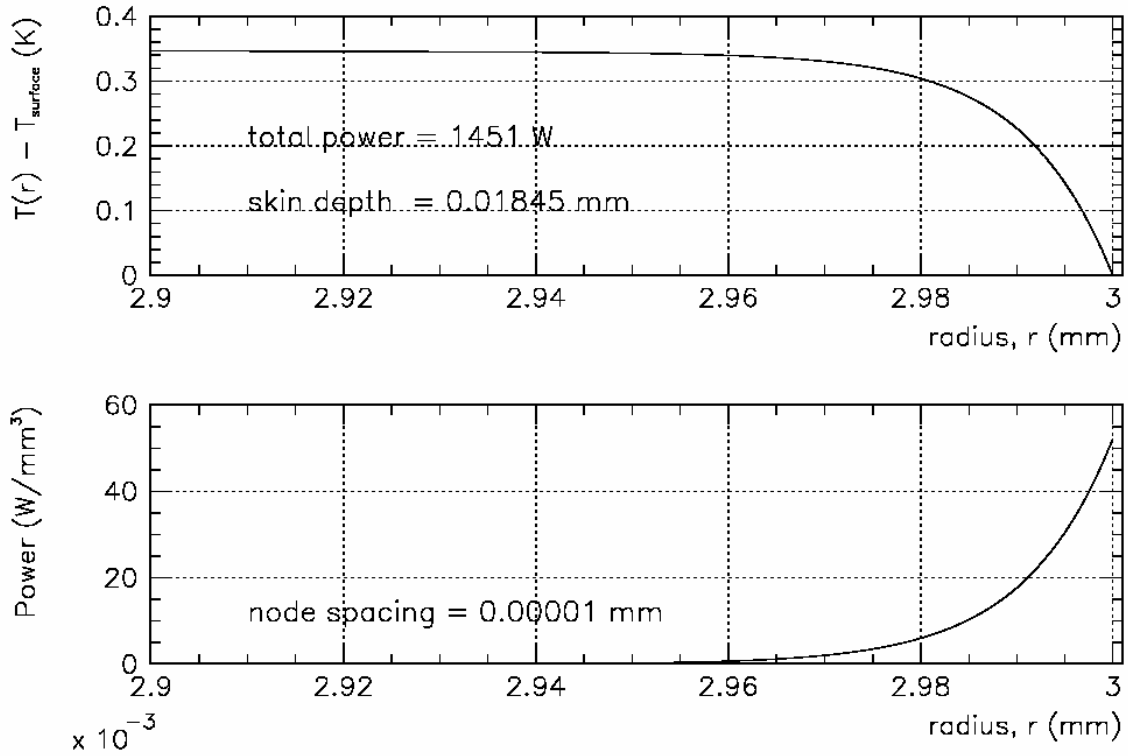

Figure 33: Target temperature (relative to that at the surface) computed solving Maxwells equations and the heat equation for induction heating. Position (horizontal axis) is measured from the target surface, for a cylinder of the same size as the target, made of permalloy. Also plotted is the actual power distribution shaped by the skin depth.

Induction heating required the coolant containment assembly to be redesigned. Delrin was the natural choice for the shell. It is a high strength plastic, used to make pump gears, and other applications that require geometrically stable parts while under heat and stress. It has a very small coefficient of expansion up to 82.2 C, with a density slightly less than water, 0.95 g/cm^3. Figure 34 shows the entire cooling unit, without the inlet and outlet fittings and plastic tubing to substitute for the 25 cm pipes. The cylindrical cavity housing the target and flow channel had to be gun drilled, since the radius had to be accurate to one mil (0.001") over approximately 6 inches. The endcaps were threaded and gasketed for a tight seal; the one at the outlet had a narrow hole drilled in it to accomodate a temperature sensor inside the target.

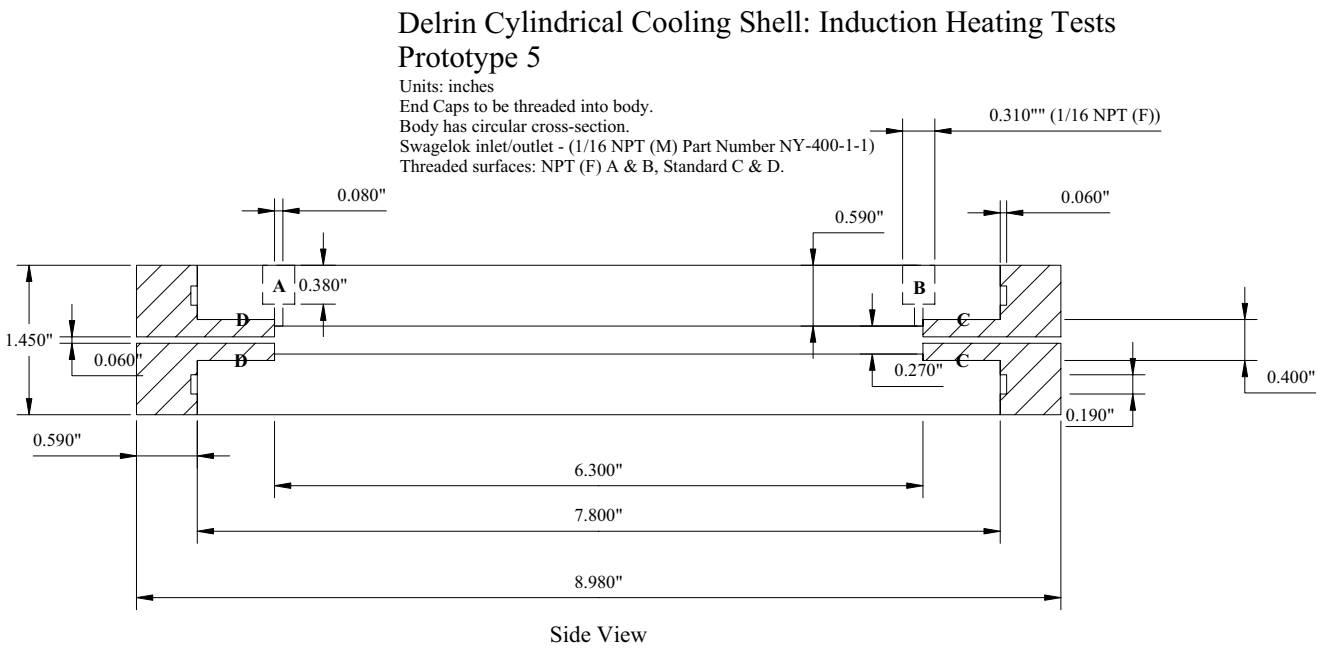

Figure 34: Design drawing of Delrin cooling shell for induction heating tests. Correction: only one endcap has a hole drilled in it. The inlet and outlet are designated by "A" and "B" and are designed to accept NPT threaded plastic compression fittings.

It is particularly important to install the target temperature sensor correctly. The primary concern was to insure that the sensor did not come in contact with coolant. The solution was to seal the sensor inside the target and endcap (which extended up to the target end). However, this raised a second concern, the rod and endcap had to be centered properly, otherwise screwing the endcap down could drag the target feet over the carefully machined target cavity wall, modifying the flow channel. Figure 35 shows a delrin tube for maintaining allignment of the cap and rod. The delrin endcap and tube, target rod, and temperature sensor are glued together as a single unit; care full attention was paid to filling all voids with glue. Note that unrelated features of the rod and cap were not included in the drawing.

Foremost in the list of tasks is to be certain power can be measured and controlled; there are three areas we have investigated which could help adjust power: power unit output control, target material choice, and coil design. As Table 5 shows, the vacuum tube model Lepel 20 power unit (rated at 20 kWatts) delivered about 15% of the power sought. Probing the field further revealed that the design frequency, 475 kHz, was unobtainable, nor was the maximum current. However, this did not prevent making the measurements listed above.[iii] Varying target materials can also increase power deposition. Target rods were machined using Iron (100% Fe), Nickle Alloy 200 (Commercially pure Ni), Nickle alloy HX (47.5% Ni, 18.5% Fe, 21.8% Cr), and Permalloy (50% Fe, 50% Ni); these were selected as most likely to attain as high a magnetic permeability as possible at high magnetic fields and frequencies. The most successful target rods were iron and Permalloy. Coil construction is also fundamental to controlling power. The coil was constructed from copper tubing with 0.635 cm OD and 0.483 cm ID (standard ¼" copper tubing), wrapped with electrical tape for insulation, and coiled tightly around the unit shown in Figure 34 from endcap to endcap; acheiving 152 turns/m. The inductance, not including the target rod is approximately 10 μH . Further improvement in coil design may be possible.

We compared three methods for measuring power: the first is entirely independent of the second and third. The manufacturer, design, and type of thermistors used in the first test were also completely different from the second and third. We will use the same notation from Figure 25 to be completely clear what sensors were used. In all cases we have not attempted to account for heat lose to the environment.

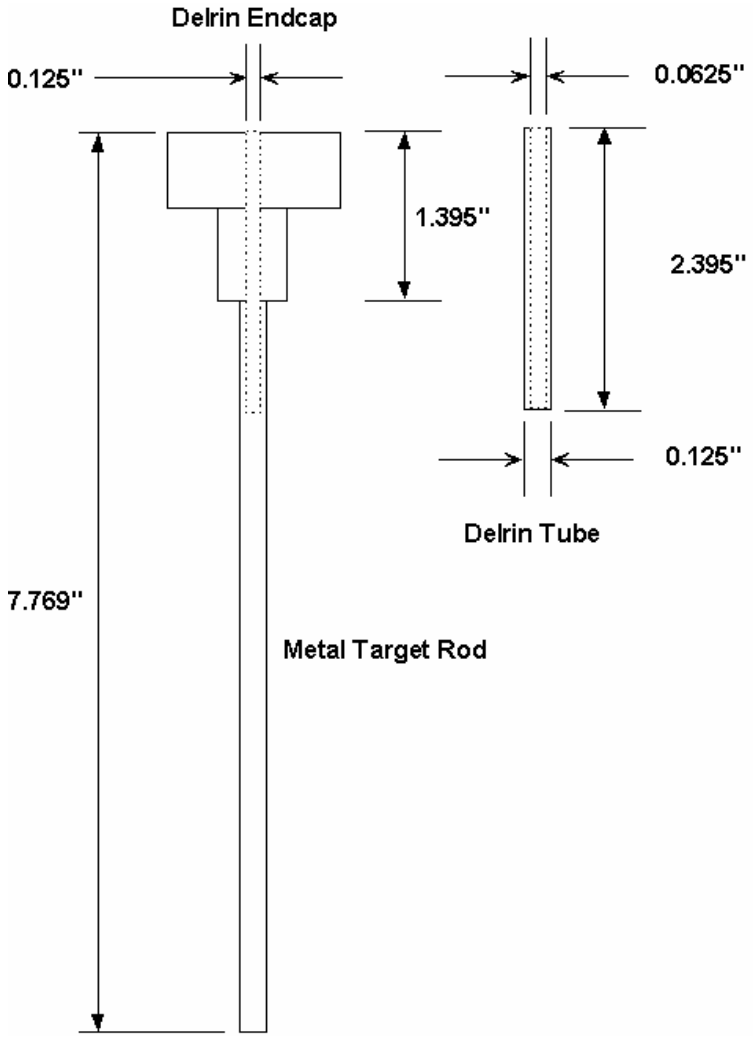

Figure 35: Target temperature sensor mounting assembly. The design shown here is slightly improved over the actual sensor assembly used in the first heating tests. The delrin tube provides proper centering and stability for the cap and rod. The tube OD was made slightly smaller and the ID slightly larger to accommodate gluing the three pieces shown and sensor together. The exact sensor tip position could be varied from 0-1" from the end for the rod.

The difference between the target inlet and outlet temperatures is the most direct measure of power; thus, $P = \rho c_p Q_{\text{hot}} (T_{\text{out}} - T_{\text{in}})$, where c_p is the specific heat of the coolant and ρ is the mass density. The streams in and out of the target were assumed fully mixed. An example of the data collected with constant power, as a function of time is given in
Figure 36. The average temperature difference was 5.5 C, in other words, 1425 Watts.

If the reservoir is suitably mixed, so that the temperature is the same throughout the reservoir, then the sensor labeled T_R can be used to measure power. The first simply uses the measured temperature rise in the reservoir (neglecting the small amount of water present in the pipes). So we have

$$P = \rho c_p V_R (T_R^{\text{final}} - T_R^{\text{initial}}) / (t_{\text{final}} - t_{\text{initial}}),$$

where "initial" and "final" refer to the times when the power unit was switched on and off. Finally, the slope in the temperature rise may also be used:

$$P = \rho c_p V_R \frac{dT_R}{dt}.$$

The results of these calculations are shown in Table 5. Given that the power unit showed some instability in output and the later revelations about the state of the device, the results from the three different calculations may be considered to be in rough agreement.

Table 5: Power deposition: First cooling tests of prototype 03 using two different target metals. The power unit was a vacuum tube model Lepel 20, designed to provide 20 kWatt at 475 kHz. However, its actual performance was significantly lower. The frequency was verified observed to be 175 kHz. The volume of water used in all tests was about V_R = 23.5 gallons

Target	Gap	Target	Power	Mean	Mean	Target	Temp	Measured	Measured	Measured	Average
	size	Rod	unit	flow	pres.	Internal	Rise	Power	Power	Power	of three
		Material	setting	rate		Temp	Difference:	Difference:	Res. Temp.	Slope of	methods
							Outlet - Inlet	Outlet - Inlet	Change	Res. Probe	
#	mm		%	gpm	psig	deg C	deg C	Watts	Watts	Watts	Watts
1	0.41	Permalloy	50	0.99	118		0.2	64	319	351	245
1	0.41	Permalloy	60	1.16	118		1.6	490	487	517	498
1	0.41	Permalloy	70	1.00	108		2.5	658	717	813	730
1	0.41	Permalloy	80	1.00		46.2	3.7	974	869	1193	1012
1	0.41	Permalloy	80	1.00			3.8	1005	1017	1211	1077
1	0.41	Permalloy	80	1.01	100		3.7	995	1058	1175	1076
1	0.41	Permalloy	90	0.99	98		4.3	1129	1197	1296	1208
1	0.41	Permalloy	100	0.98		54.1	5.5	1428	1324	1331	1361
1	0.41	Permalloy	100	0.99		53.0	5.8	1518	1379	1412	1436
1	0.41	Permalloy	100	0.99		42.3	5.4	1408	1343	1278	1343
3	0.30	Iron	100	0.93	201		6.5	1601	1740	1587	1643

Target surface temperature was straight-foreward to measure. The target sensor was a thermistor encased in the epoxy used to assemble the target, endcap, centering tube, and sensor into a single unit. It was confirmed that the sensor wires were not shorted with the target. Due to pressure limitatioms of the plastic water containment shell, cooling tests were performed with a 0.4 mm gap rather than 0.3 mm, for the most part. The sensor was positioned 1.9 cm in from the target end (In future this will be made smaller). The coolant conditions were 1.0 gpm and with a pressure drop across the target of 125 psi for the Permalloy tests at 100% power. The difference between the target temperature and the inlet water temperature is shown in Figure 37. The average difference is $T^0_{\text{target}} - T^0_{\text{target}} = 21.0\,\text{C}$, with a target power of about $P^0_{\text{target}} = 1425\,\text{Watts}$. A close upper limit to target outlet surface temperature can be gotten from the expression for other power levels: $T^1_{\text{surface}} = T^1_{\text{in}} + (T^0_{\text{target}} - T^0_{\text{in}}) \frac{P^1}{P^0_{\text{target}}}$.

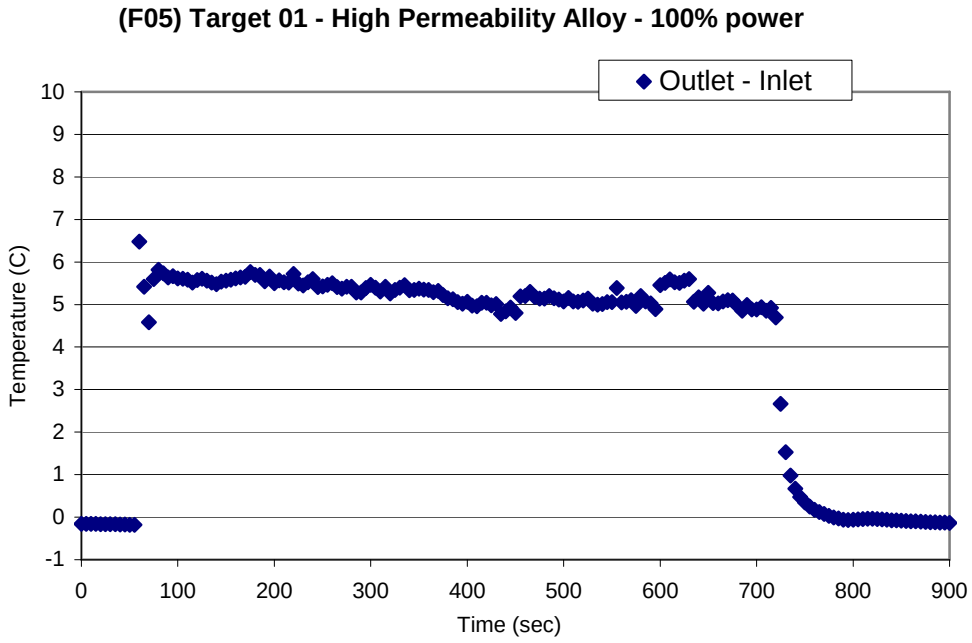

Figure 36: Power deposition measurement for Permalloy – Carpenter high permeability alloy 49. The sensors, T_{in} and T_{out}, were identical. The average step in temperature is approximately 5.5 C, with a flow rate of 0.98 gpm.

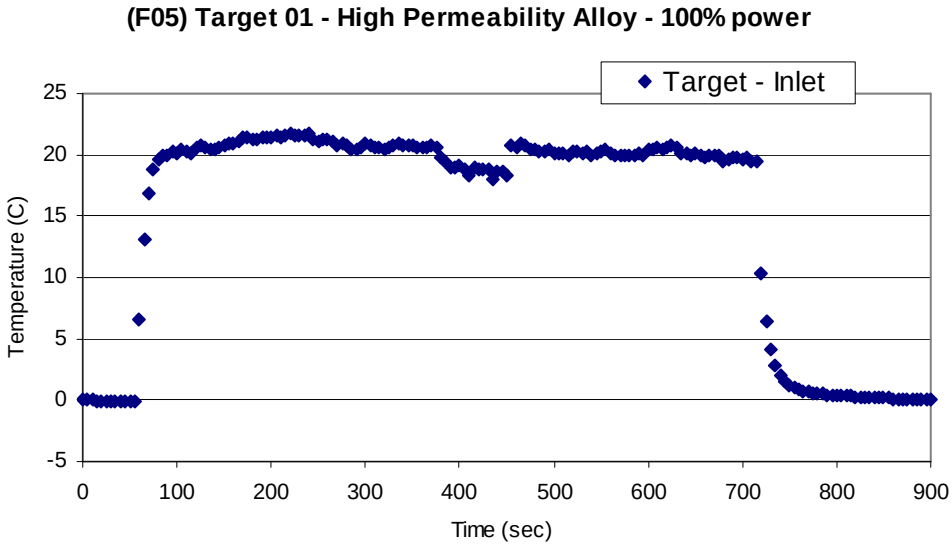

Figure 37: Upper limit to the target surface temperature minus the inlet temperature of the coolant.

Scaled up to MECO, $P^1_{\text{target}} = 7550$ Watts, we have $T^1_{\text{surface}} = T^1_{\text{in}} + 111.0\,\text{C}$. Figure 16 assumes an inlet coolant temperature of 20 C. Even though outlet surface temperature is certainly below the likely temperature limit, MECO would not run underthese conditions. The iron target had a gap of 0.3 mm, flow rate 0.93 gpm, and pressure drop 201 psi. The target-inlet temperature difference is $T^0_{\text{target}} - T^0_{\text{target}} = 9.5\,\text{C}$; scaling to MECO we have $T^1_{\text{surface}} = T^1_{\text{in}} + 42.0\,\text{C}$. To compare to Figure 16, we must scale to $P^1_{\text{target}} = 9500$ Watts, yielding $T^1_{\text{surface}} = T^1_{\text{in}} + 53.3\,\text{C}$; however, our cooling calculations suggest only a 40 C rise. Gap size, flowrate, and coolant speed are closely related. The larger gap size most certainly lead to lower coolant speeds and thus higher surface temperatures. However, there is a crucial performance-reducing feature that became evident more slowly.

Close examination of the Delrin shell with revealed that the inlet and outlet fittings were miss-aligned with the inlet and outlet holes drilled through to the target cavity. The difference was slight, but we have learned that steps, rather than smooth transitions, lead to vortex motion and dead zones, which ultimately narrow the flow channel at the geometrical transition and slow the fluid down. The effect was sever enough to cause some visible cavitation. Ultimately, a different approach to mating the compression fittings to the shell will be required before the next round of cooling tests.

1.6 Installation and Removal

Figure 38 shows the all-titanium target shell and service pipe assembly fully in place in the Production Solenoid. The system rigidity is due to the metal cross braces spaced along the large diameter pipes. The braces are shaped to fit into the dovetail slot cut out of the heat shield, which supports the target assembly securely. The sensitivity of target position under normal heating conditions is currently under study. However, prototype tests using a "non-pulsing" rotary vane pump and slightly longer inlet/outlet and support pipes, indicate that coolant circulation without heating does not cause significant vibrations.

Over the lifetime of the MECO facility the production target will require periodic disassembly and detailed mechanical inspection. In addition, spent targets require removeal & storage, and replacement units installed. Target manipulation will be accomplished using a simple robotic arm mounted on the shielding blocks forming the roof over the Production Solenoid. Once in position, there are three main steps to target installation, shown in Figure 39 through Figure 41, below.

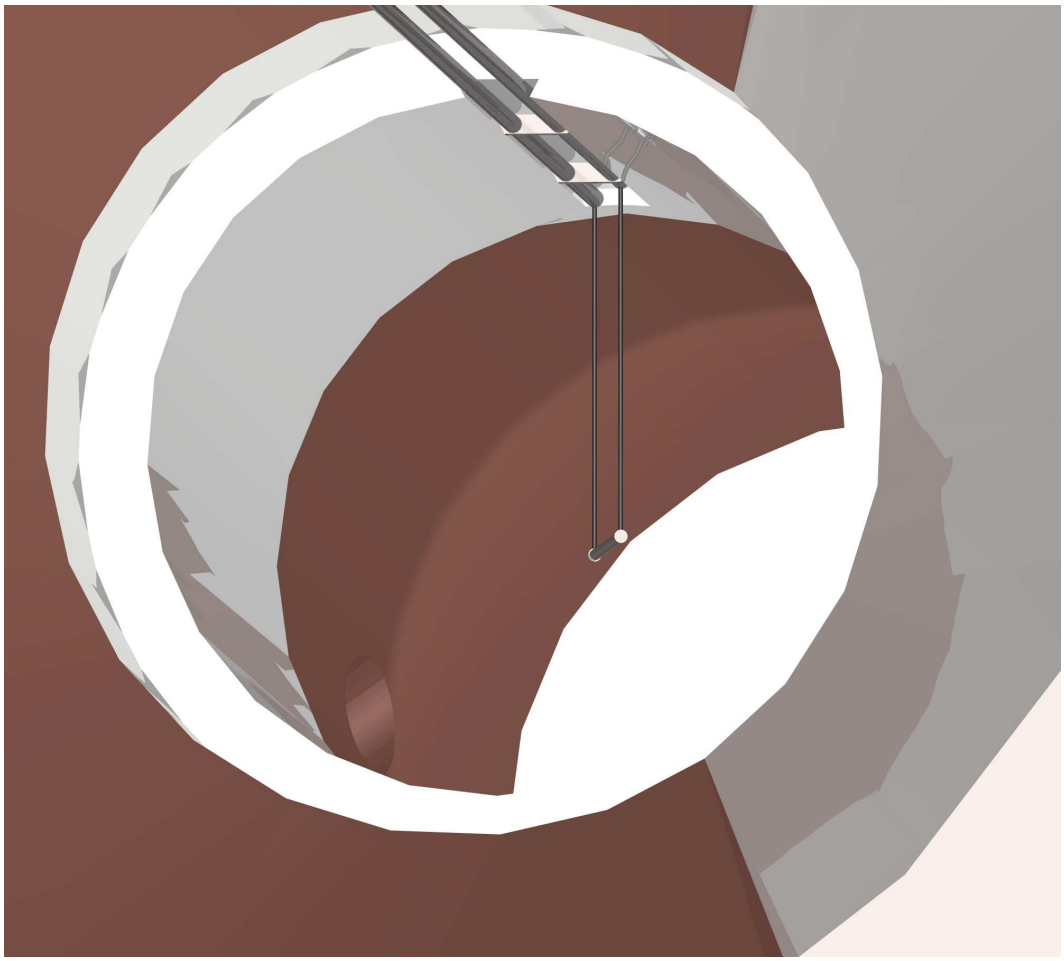

Figure 38: Target & service pipes fully installed. The target assembly is made rigid with steel cross braces between the larger diameter service input and return pipes. Hanging in a dovetail slot cut out of the heat shield supports the arrangement.

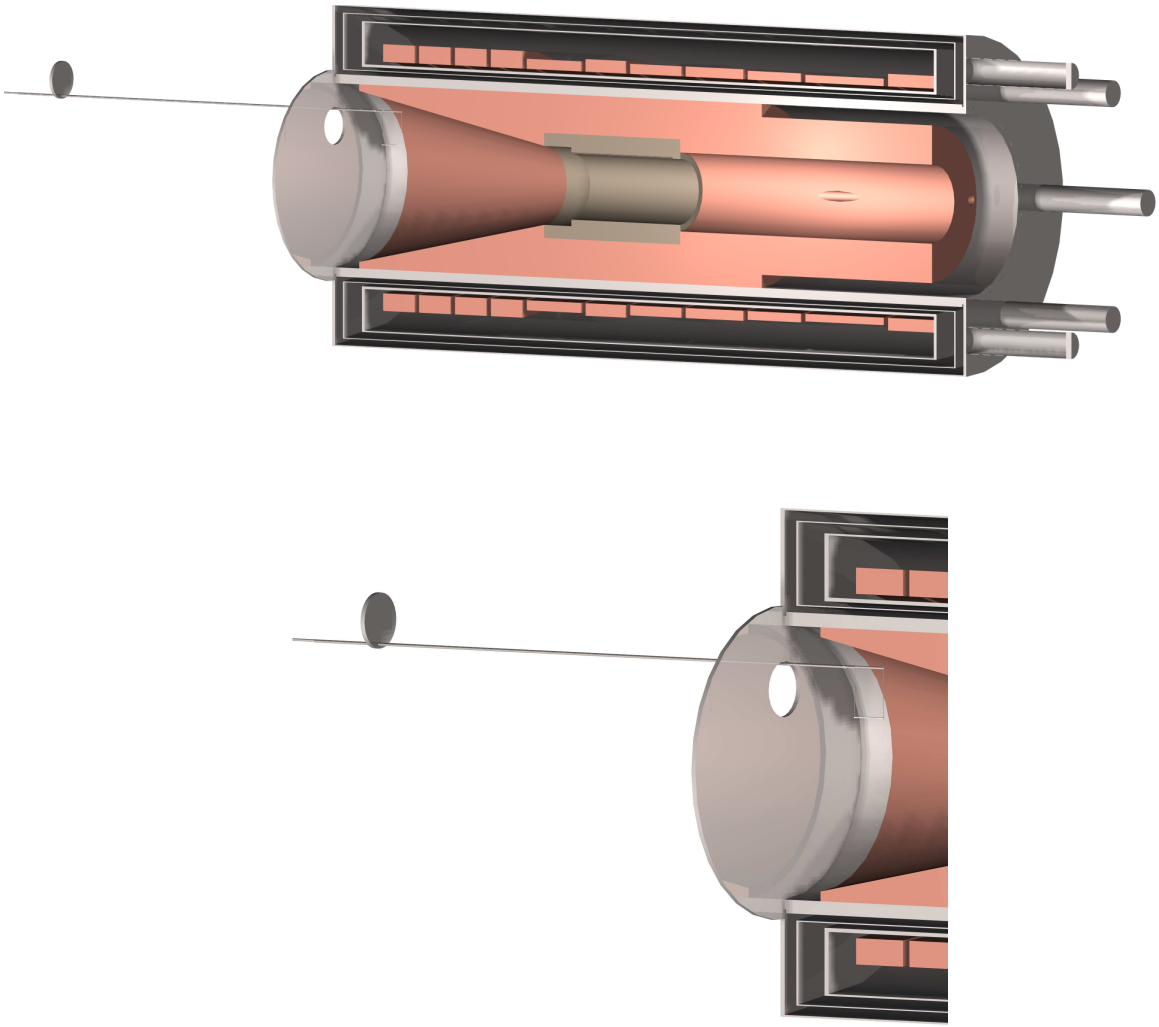

Figure 39: Step 1, target insertion through vacuum port. Top shows entire production solenoid; bottom only the down-stream end of the top picture; the target is more clearly visible.

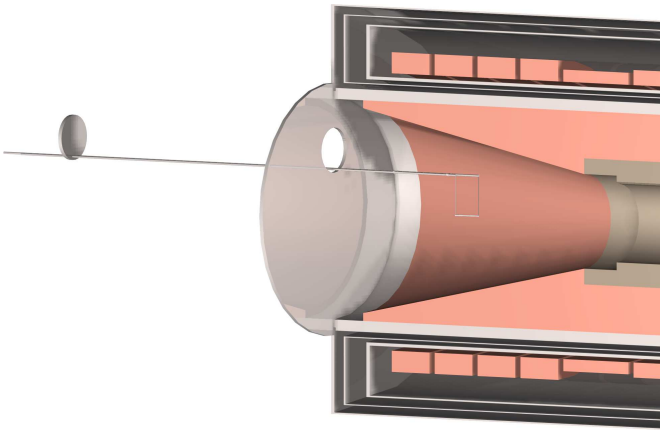

Figure 40: Step 2, lowering the target & service pipe structure to line up with the dovetail slot in the shield.

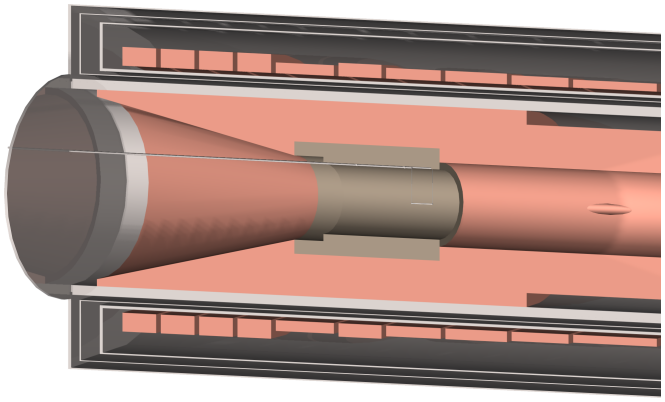

Figure 41: Step 3, target in final position and vacuum port closed.

Step 1 of installation is completed once the target assembly is brought into the orientation shown in Figure 39; in this case, the target undergoes a single horizontal translation, with the target passing through the vacuum port and finally positioned just inside the port. Step 2 is a linear translation downwards, until the large-diameter service pipes rest on the bottom edge of the port and the first crossbrace on the upstream end of the large pipes is lined up with the dovetail slot. Step 3 is a linear translation parallel to the solenoid axis. This step is complete when the leading crossbrace reaches the end of the slot, and the vacuum plate is sealed.

1.7 References

1. Djilkibaev, R. and V.Lobashev, Sov. J. Nucl. Phys., 1989. **49**(2): p. 384.
2. Abadjev, V.S., et al., *MELC Experiment to search for the $\mu^- A$ to $e^- A$ Process.* 1992.
3. Palmer, R., et al., Nucl. Phys. Proc. Suppl., 1996. **51A**: p. 61.
4. Bachman, M., et al., *A Search for $\mu^- N \rightarrow e^- N$ with Sensitivity Below 10^{-16}*. 1997, Brookhaven National Laboratory: Upton, NY.
5. Armutliiski, D., et al., *Hadron Spectra in Hadron-Nucleus Collisions*. 1991, Preprint submitted to Sov. J. Nucl. Phys.
6. Djilkibaev, R., *Pion Yield and Muon Flux Simulation*. 1997, New York University.
7. Bachman, M. and R. Lim, *Pion Yield and Muon Flux Simulation*. 1997, University of California, Irvine.
8. Brun, R., et al., *Program GEANT3*. 1984, CERN.
9. Tumakov, V., *Comparison of the Muon Yield and Energy Deposition in the Target for Different Proton Target Design*. 2001, University of California, Irvine.
10. Pai, C. and J. Popp, *Review of Thermal Stresses in a Radiation-Cooled Target for MECO*. 2003, University of California, Irvine.
11. Tumakov, V., *Simulation of the Tritium Production in the Water Cooled Target*. 2002, University of California, Irvine.
12. Davies, J. and P. Simpson, *Induction Heating Handbook*. 1979, London: McGraw-Hill. 426.
13. Warren, A.G., *Mathematics Applied to Electrical Engineering*. 2 ed. Monographs on Electrical Engineering, ed. H.P. Young. Vol. 9. 1958, London: Chapman & Hall LTD. 324.
14. Tranter, C.J., *Bessel Functions with Some Physical Applications*. 1968, London: The English Universities Press LTD. 148.

---

[i] Alpha Laval; US representative: Air Treatment Corporation, 807 South Lemon Avenue, Walnut, CA 91789, 949-831-3260, (FAX) 949-349-0304, http://alphalaval.com, jpedersen@airtreatment.com. Lytron, Inc., 55 Dragon Court, Wobum, MA 01801, 781-933-7300, http://www.lytron.com, brollins@lytron.com.

[ii] Teel carbonator-mount rotary vane pump, 316 stainless steel body, max. pressure 240 psi, max. temperature 70 C; Dayton capacitor-start C-face ¾ hp electric motor.

[iii] Induction Heat Treet, Co., Huntington Beach CA, used the Lepel 20kWatt unit on their shop floor, daily; however, demands on its specific performance wer rare, if at all. Its owners deemed this fifty-year old equipment reliable. The decline in performance was unknown to them; our work actually brought it to their attention. Service personel confirmed our conclusions and it was deemed more economical to retire this particular unit rather than repair it.